

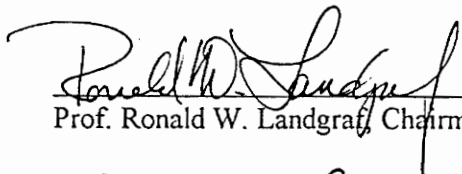
CONTACT STRESS ANALYSIS AND FATIGUE LIFE PREDICTION FOR A CAM-ROLLER FOLLOWER SYSTEM

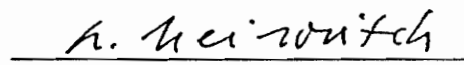
by

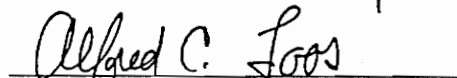
Benoit Girardin


Thesis submitted to the Faculty of the
Virginia Polytechnic Institute and State University
in partial fulfillment of the requirements for the degree of
MASTER OF SCIENCE
in
Engineering Science and Mechanics

APPROVED:


Prof. Ronald W. Landgraf, Chairman


Prof. Leonard Meirovitch


Prof. Alfred C. Loos


Prof. Norman S. Eiss

June, 1994

Blacksburg, Virginia

C.2

LD
5655
V855
1994
G573
C.2

CONTACT STRESS ANALYSIS AND FATIGUE LIFE PREDICTION FOR A CAM-ROLLER FOLLOWER SYSTEM

by

Benoit Girardin

Committee Chairman: Ronald W. Landgraf
Engineering Science and Mechanics

(ABSTRACT)

An analytical treatment of the fatigue performance of a cam-roller follower system as influenced by residual stresses induced by grinding, is developed. An approach based on an extended Hertzian analysis is used to determine the 3-D contact stress fields, which are then combined by elastic superposition with the residual stress fields. These residual stresses were measured previously by the x-ray diffraction technique and represent a range of grinding protocols from mild to abusive.

The maximum cyclic component, generally occurring subsurface, is then identified in terms of an effective stress amplitude and mean which are used with a fatigue damage model to predict fatigue crack initiation. Results, pending experimental confirmation, appear reasonable and provide a useful basis for optimizing cam performance in terms of manufacturing and design parameters.

ACKNOWLEDGMENTS

Financial support for this research was provided under the National Science Foundation Strategic Manufacturing Initiative project #230-11-110F-108-323622-1.

I would like to thank my advisor, Dr. R.W. Landgraf, for his support and help throughout this work, Dr. N.S. Eiss, Dr. A.C. Loos and Dr. L. Meirovitch for their time and interest, as well as Dr. N.E. Dowling and Dr. R.W. Hendricks.

I wish to express my gratitude to Dr. J.R. Mahan, coordinator of the exchange program between Virginia Tech and the Université de Technologie de Compiègne (France), that permitted me to enroll the Master's program of the Engineering Science and Mechanics department.

Special thanks are due to colleagues I worked with everyday : Robbie Cunningham, Dilip Vijay, Scott Courtney, Mike Stawovy, Greg Moeller, Heidi Allison and Robin Ott.

“Grand Merci” to the “French connection” which was here everyday during these two years in Blacksburg : Delphine Jestin, Anne-Claire Christiaen, Anne Vilette and Eric Toffin, and to my American friends : Bob Smith, Robert Bennett, Mike Pastor and Jim Dolan.

Finally, I would like to thank all my family, my parents and grand-parents, for their encouragement and support during all my studies.

TABLE OF CONTENTS

1. INTRODUCTION.....	1
2. BACKGROUND	4
2.1 CONTACT STRESSES.....	4
2.2 HERTZIAN THEORY	4
2.3 PLASTICITY.....	6
2.4 FATIGUE ANALYSIS.....	8
2.5 RESIDUAL STRESS FIELDS	10
3. STRESS ANALYSIS.....	13
3.1 CONTACT STRESSES - CASE OF TWO PARALLEL CYLINDERS	13
3.1.1 Area of contact and pressure distribution	13
3.1.2 Limitations of the Hertzian method	15
3.2 DETERMINATION OF THE CONTACT STRESSES.....	16
3.2.1 Study of two cases	16
3.2.1.1 Plane stress.....	16
3.2.1.2 Plane strain.....	17
3.2.2 Plane stress.....	17
3.2.2.1 Stresses in depth.....	18
3.2.2.2 Maximum values of the different stresses.....	19
3.2.3 Plane strain	22
3.2.4 Principal stresses	22
3.3 RESULTS.....	24
3.3.1 Plane stress.....	24
3.3.2 Plane strain	29
3.3.3 Principal stresses.....	30
3.4 RESIDUAL STRESSES (RS).....	33
3.4.1 Actual stress field	36
3.4.2 Maximum shear stress.....	39
4. PLASTICITY.....	41
4.1 CRITERIA.....	41
4.1.1 Tresca criterion	41
4.1.2 Von Mises criterion.....	42
4.2 RESULTS OF THE CRITERIA COMPUTATIONS	44
4.3 STRESS RELAXATION	48
4.4 RESULTS OF THE RELAXATION.....	50
5. LIFE PREDICTIONS.....	54
5.1 FATIGUE MODELS	54
5.1.1 Morrow model.....	55

5.1.2 Smith Watson Topper model (SWT).....	55
5.1.3 Socie model.....	56
5.2 SELECTION OF THE MOST DAMAGED PLANE.....	58
5.3 RESULTS OF THE LIFE PREDICTION	59
5.3.1 Smith Watson Topper.....	59
5.3.2 Socie	60
5.3.3 Morrow	61
5.3.4 Von Mises effective stress.....	64
5.3.5 Assembly residual stress field	65
6. DISCUSSION	68
7. CONCLUSIONS	75
7.1 CONCLUSIONS.....	75
7.2 RECOMMENDATIONS	77
8. REFERENCES.....	78
9. APPENDIX A : MATERIAL PROPERTIES OF AISI 52100	80
10. APPENDIX B : RESIDUAL STRESS GRAPHS	81
11. APPENDIX C : TABLES OF PREDICTED SERVICE LIVES.....	85

LIST OF FIGURES

Figure 1-1: Valve train model.....	2
Figure 1-2: (a) Flat-faced follower and (b) roller follower [Engineering Science data].....	3
Figure 2-1: Pressure distribution between two curved bodies in contact [Juvinal].	5
Figure 2-2: Monotonic and cyclic stress - strain curves of AISI 52100.....	7
Figure 2-3: Example of relaxation of the mean stress ²⁰	8
Figure 2-4: Strain - life curve for the steel AISI 52100 ¹⁴	9
Figure 2-5: Lobe nomenclature(0°:nose, 60°:opening ramp, 180°:base circle, 300°:closing ramp) [Courtney].....	11
Figure 2-6: Different directions of measurement along camshaft [Courtney].	11
Figure 2-7: Axial residual stresses vs. depth on the base circle for several lobes [Courtney].....	12
Figure 3-1: Contacting parallel cylinders [Hearn].....	13
Figure 3-2: Contact pressure distribution [Juvinal].	14
Figure 3-3: Example of Mohr's circle for (a) plane stress and (b) plane strain conditions.	16
Figure 3-4: Plane stresses in the y-z plane.....	17
Figure 3-5: Normal stress (a) in the y-direction and (b) in the z-direction over the contact area at different depths [Juvinal].	20
Figure 3-6: Shear stress in the y-z plane over the area of contact at different depths [Juvinal].	21
Figure 3-7: Directions of the plane stresses going through the area of contact [Juvinal].	21
Figure 3-8: Normal stress in the x-direction over the area of contact for different depths [Juvinal].	22
Figure 3-9: Maximum values of the normal stresses (a) σ_y and (b) σ_z vs. depth for different locations around the cam lobe, considering several ratios R_f/R_c ($R_c = 12$ mm).....	25
Figure 3-10: Maximum values of τ_{yz} vs. depth for different locations around the cam lobe, considering several ratios R_f/R_c ($R_c = 12$ mm).....	26
Figure 3-11: Plane stresses over a range $-4b$ to $4b$ along the y-axis at a depth $z = b/8$ on the base circle with $p_0 = 220$ ksi.....	27
Figure 3-12: 3-D graph of σ_y vs. y and depth on the base circle.	28
Figure 3-13: 3-D graph of σ_z vs. y and depth on the base circle.	28
Figure 3-14: 3-D graph of τ_{yz} vs. y and depth on the base circle.	29
Figure 3-15: 3-D plot of σ_x vs. y and depth on the base circle.....	30
Figure 3-16: Example of the rotation of the principal directions at a depth $b/4$ over the first part of a cycle ($-1.5b < y < 0$).	31
Figure 3-17: Surface residual stress around cam (0°: nose, 60°: opening ramp, 180°: base circle, 300°: closing ramp) in the axial direction [Courtney].	34
Figure 3-18: Residual stress in the (a) axial and (b) circumferential direction on the ramp for several lobes [Courtney].	35
Figure 3-19: (a) Contact stress and (b) residual stress fields on the base circle vs. depth.....	37
Figure 3-20: Actual stress fields over a range $-4b$ to $4b$ along the y-axis at a depth $z = b/8$ for the base circle of (a) the burned and (b) the unburned lobes.	38
Figure 4-1: Yield surfaces in the two dimensional stress system [Liebowitz].	42
Figure 4-2: (a) Effective Tresca stress and (b) effective von Mises stress over a range of maximum Hertzian pressure from 200 ksi to 300 ksi at a depth of $0.2b$ for several cases.	45
Figure 4-3: Effective (a) Tresca and (b) von Mises stresses over a range of maximum Hertzian pressure from 200 ksi to 300 ksi at a depth of $0.75b$ for several cases.	46

Figure 4-4: Example of a stress cycle.	48
Figure 4-5: Effective Tresca stress on the base circle of the (a) burned and (b) unburned lobes over a range from $-4b$ to $4b$ on the y-axis at different depths.	51
Figure 4-6: Relaxation of the mean stress on the base circle of the (a) burned and (b) unburned lobes for different depths.	52
Figure 5-1: Maximum shear stress and associated normal stress around a crack [Socie].	56
Figure 5-2: Morrow's model predictions on the base circle vs. the maximum Hertzian pressure for several cases.	62
Figure 5-3: Morrow's predictions (a) on the nose (b) on the ramp vs. the Hertzian pressure for several cases.	63
Figure 5-4: Morrow life predictions on the base circle of lobe 2 vs. the maximum Hertzian pressure, using Tresca and von Mises effective stress.	64
Figure 5-5: Residual stresses in the circumferential direction for lobe 4 and 6 and for Ford data which consider the assembly residual stresses.	66
Figure 5-6: Morrow's model predictions on the base circle of lobe 4 and 6 with or without the assembly residual stresses, for a range of maximum Hertzian pressure between 200 ksi and 300 ksi.	66
Figure 6-1: Life predictions according to Morrow model as a function of the grinding conditions and the maximum Hertzian pressure (a) on the base circle, (b) on the ramp and (c) on the nose.	71
Figure 6-2: Loads around the cam lobe caused by the valve train for two camshaft rotation speeds.	72
Figure 10-1: (a) Axial and (b) circumferential residual stresses vs. depth on the nose of the different lobes [Courtney].	82
Figure 10-2: (a) Axial and (b) circumferential residual stresses vs. depth on the ramp of the different lobes [Courtney].	83
Figure 10-3: (a) Axial and (b) circumferential residual stresses vs. depth on the base circle of the different lobes [Courtney].	84

LIST OF TABLES

Table 3-1: Residual stress tensors on the base circle for several lobes [Courtney].....	33
Table 3-2: Number of grinding passes and depth of cut per grinding pass [Courtney].....	34
Table 3-3: Location and magnitude of the highest maximum shear stress in the case of the base circle with $p_0 = 220$ ksi.	40
Table 5-1: Life prediction from Socie's model on the base circle of lobe 2 over a range of Hertzian pressure from 200 ksi to 300 ksi.	60
Table 5-2: Life predictions from Morrow parameter at the base circle for (a) lobe 2, (b) lobe 8 and (c) no residual stresses over a range of maximum Hertzian pressure from 200 ksi to 300 ksi.....	61
Table 6-1: Failure locations below the surface on the base circle over a range of pressure between 200 ksi and 300 ksi for the different lobes.	71
Table 6-2 : Structure of the routine developed.	74
Table 11-1: Service life predictions from Morrow model on the nose.	85
Table 11-2: Service life predictions from Morrow model on the ramp.	86
Table 11-3: Service life predictions from Morrow model on the base circle.	87
Table 11-4: Service life predictions from Morrow model using von Mises effective stress on the nose of lobe 2.	87

1. INTRODUCTION

Major efforts are currently underway in industry to better understand the effects of manufacturing processes on component performance. Fatigue performance is of particular interest because of its sensitivity to a host of processing variables. Increased understanding and control of these variables could lead to more optimized service performance.

The work presented herein is focused on the cam of an automobile engine. The cam opens and closes the valves through the valve-train (see Figure 1-1), by rotation of the camshaft. The cam may be in contact with a flat-faced follower or a roller follower, as illustrated by Figure 1-2. The flat-faced follower entails friction loads, while the roller follower, because of rolling contact with the cam, generates only normal loads. In that case, the cam is subject to a fatigue failure due to the cyclic stresses induced by each revolution of the shaft. Traditionally, camshafts were made of cast iron; more recently, in order to reduce weight problems and improve performance, cam lobes are now pressed onto a tubular shaft, after going through a series of complex manufacturing operations involving hot forging, induction hardening, tempering and grinding. While all these processes may affect the fatigue life, grinding is of particular importance because of the residual stress fields created in the cam lobe subsurface.

This study is part of an ongoing three-year investigation of cam lobe grinding protocol sponsored by the National Science Foundation, with participation from Ford Motor Company, Litton Landis (grinding equipment), General Electric (grinding wheel abrasive) and American Stress Technologies (residual stress measurements). The goal of this project is to understand and hence control the performance of camshafts through appropriate manufacturing procedure. The

individual tasks to be performed are:

- Generation of residual stress fields by grinding under different protocols
- Measurement of residual stresses and stress gradients
- Computation of temperature and stress distributions
- Measurement of thermal effects
- Effect of residual stresses on service performance

Some of these have already been accomplished, while others are in progress.

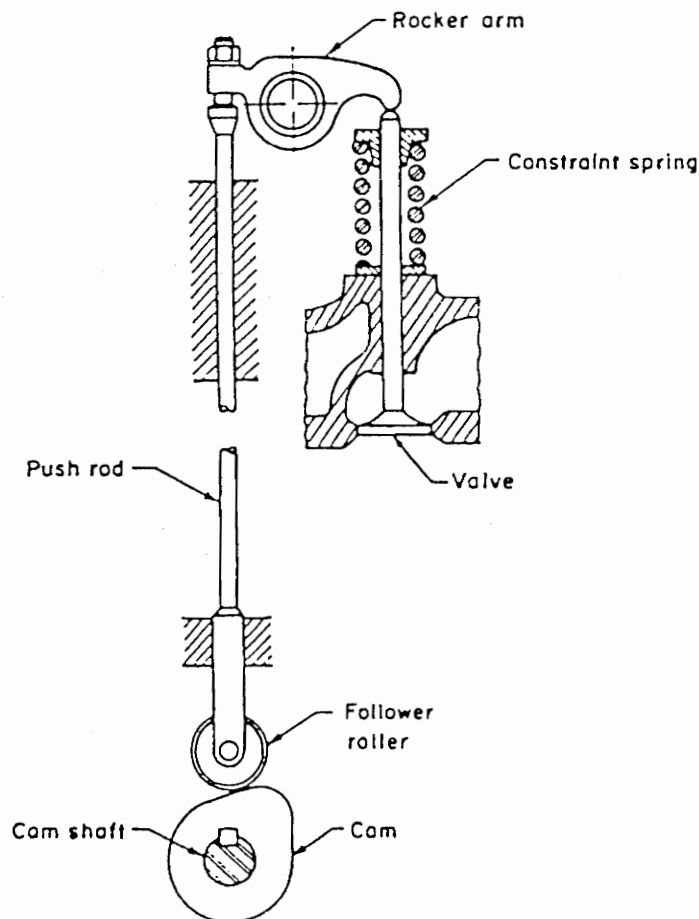


Figure 1-1: Valve train model.

The present work deals with the effect of residual stresses on service performance. The elements needed to predict the fatigue life are :

- Characterization of the multiaxial compressive stress field between the two bodies in contact
- Determination of the cyclic stresses in the cam
- Consideration of the residual stress fields due to grinding
- Evaluation of the possible yielding
- Development of an appropriate fatigue model for compressive stress fields

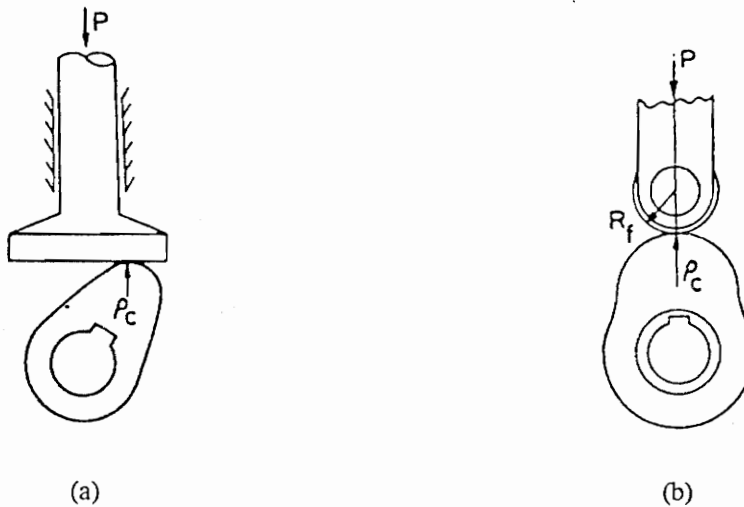


Figure 1-2: (a) Flat-faced follower and (b) roller follower [Engineering Science data].

The major goal of this task is to combine these elements into a reliable predictive model that will account for all manufacturing and performance parameters. The validity of this model is to be verified using a standard laboratory cam fatigue test system, called SVI*. This model is intended to provide a basis for improved design tools useful for optimizing cam performance as well as for other contacting mechanisms such as gears and bearings.

* From the Specialized Vehicles Inc. company which distributes them.

2. BACKGROUND

2.1 Contact stresses

The first scientist concentrating on contact stresses was H.R. Hertz¹ about one century ago. He developed an elastic theory to compute the pressure and the shape of the area of contact between two curved bodies. This early work was extended by Smith and Liu² who characterized the stress field due to tangential and normal loads, in contact problems. Moyar and Morrow³ applied this analysis principally to bearings and gears, and Littman and Widner⁴ showed that failure occurs and propagates subsurface in such components.

Currently, analytical methods and finite element analysis are used to evaluate contact stresses, especially for the contact between bodies of finite dimensions (Keer and Mura⁵ and de Mul and Kalker⁶) to model the stresses at the edge of the solid. Experimental techniques are also still considered, such as photoelasticity (Shukla and Nigam⁷), to compute contact stress fields. Other trends in this domain are oriented towards understanding the behavior of the material during this rolling contact (Hahn and Bhargava⁸) in order to identify relevant deformation and failure mechanisms.

2.2 Hertzian theory

Contact stresses are local compressive stresses developed between two contacting bodies and are the cause of damage and failure in many systems. Examples include gears, bearings, rails and cams. The Hertzian method is used to study these contact problems. Following is a brief summary of the general case of contact between two curved bodies; more details can be found in Hearn⁹ and Juvinal¹⁰.

The two curved bodies considered are assumed to exhibit elastic and isotropic behavior. The contacting surface is an ellipse, with major axis equal to $2a$ and minor axis to $2b$. The pressure distribution on this contact area can be represented as a semi-ellipsoid, as shown on Figure 2-1. The

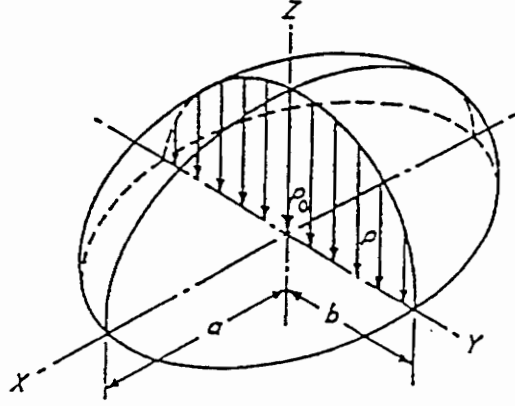


Figure 2-1: Pressure distribution between two curved bodies in contact [Juvinall].

maximum Hertzian pressure, p_0 , occurs in the middle of this contacting surface, and the pressure at any point (x, y) on this surface can be determined from:

$$p = p_0 \sqrt{1 - \frac{x^2}{a^2} - \frac{y^2}{b^2}} \quad (2.1)$$

where p_0 is given by:

$$p_0 = \frac{3P}{2\pi ab} \quad (2.2)$$

where P represents the load and the values of a and b are computed as follows:

$$a = m \left[3\Delta \frac{P}{4A} \right]^{1/3} \quad b = n \left[3\Delta \frac{P}{4A} \right]^{1/3} \quad (2.3) \text{ \& } (2.4)$$

where m , n and A are functions of the geometry, especially the radii of the contacting bodies, and Δ is a function of the elastic constants of the materials in contact, given by:

$$\Delta = \frac{1 - \nu_1^2}{E_1} + \frac{1 - \nu_2^2}{E_2} \quad (2.5)$$

where E_1 and E_2 are the Young's moduli, and ν_1 and ν_2 are the Poisson's ratios of the two materials. Therefore by knowing the geometry of the two bodies, their material properties and the

load, the area of contact, the pressure distribution and the maximum Hertzian pressure, p_0 , can be easily found.

Our work involves a cam lobe and a roller follower, so the particular case of two parallel cylinders is used, as will be described in Chapter 3. In this case, the radii have an important role because they have a direct effect on stresses, i.e. as the radius is decreased, the contact stresses increase. Moreover, in this cam-follower system, the cam is subject to a dynamic loading situation. These loads change according to the speed of rotation and the geometry of the cam. From the Hertzian analysis results, a complete mapping of the contact stress field was developed by Smith and Liu². It is found that in a contact stress field, the maximum shear stress associated with fatigue mechanisms, is subsurface.

2.3 Plasticity

The Hertzian analysis only includes elastic deformation, so it must be assured that the elasticity limit is not exceeded at any point. Thus, once the contact stresses are known, the principal stresses are computed and used in conjunction with appropriate yield theories, such as Tresca or von Mises^{11,12,13}, to determine if yielding has occurred.

Because rolling contact is a cyclic problem, the original stress-strain properties can be changed by cyclic deformation, particularly for the steel used in this work, AISI 52100, which exhibits cycle softening. To account for this effect a cyclic yield strength is defined which in this case is about 2/3 of the monotonic yield strength, as can be seen on Figure 2-2. The cyclic stress-strain curve in this figure can be characterized by¹³:

$$\frac{\Delta \varepsilon}{2} = \frac{\Delta \varepsilon_e}{2} + \frac{\Delta \varepsilon_p}{2} = \frac{\sigma_a}{E} + \left(\frac{\sigma_a}{K'} \right)^{1/n'} \quad (2.6)$$

where ε_e and ε_p are the elastic and plastic strains respectively,

σ_a is the stress amplitude,

E is the Young's modulus of the material, and

K' and n' are cyclic properties of the material.

Therefore, it is necessary to check both yield limits: the monotonic for initial yield and the cyclic for cyclic yield.

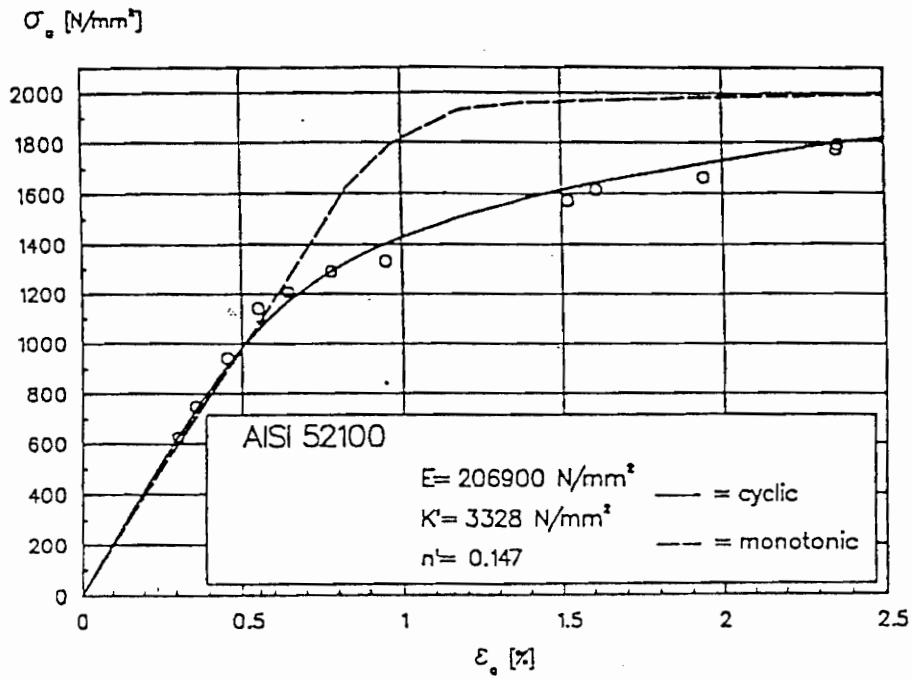


Figure 2-2: Monotonic and cyclic stress - strain curves of AISI 52100¹⁴.

Moreover, residual stresses when subject to cyclic loads, are often modified by mean stress relaxation which is a decrease in the magnitude of the mean stress, as illustrated by Figure 2-3. So a relaxation model is used to characterize this behavior. This analysis concerning plasticity and relaxation is done in Chapter 4.

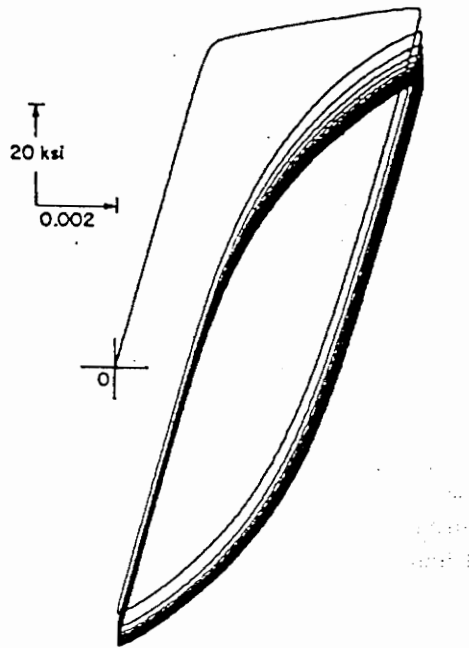


Figure 2-3: Example of relaxation of the mean stress²⁰.

2.4 Fatigue analysis

Fatigue is a cyclic mechanism, which by local plastic deformation leads to failure. Numerous models try to represent this mechanism. The fatigue characteristics of a specific material are represented by a stress-life curve (also known as S-N curve) or a strain-life curve which is more appropriate to handle plastic deformation. The strain-life curve for AISI 52100 which is obtained by running cyclic loading tests, is shown in Figure 2-4.

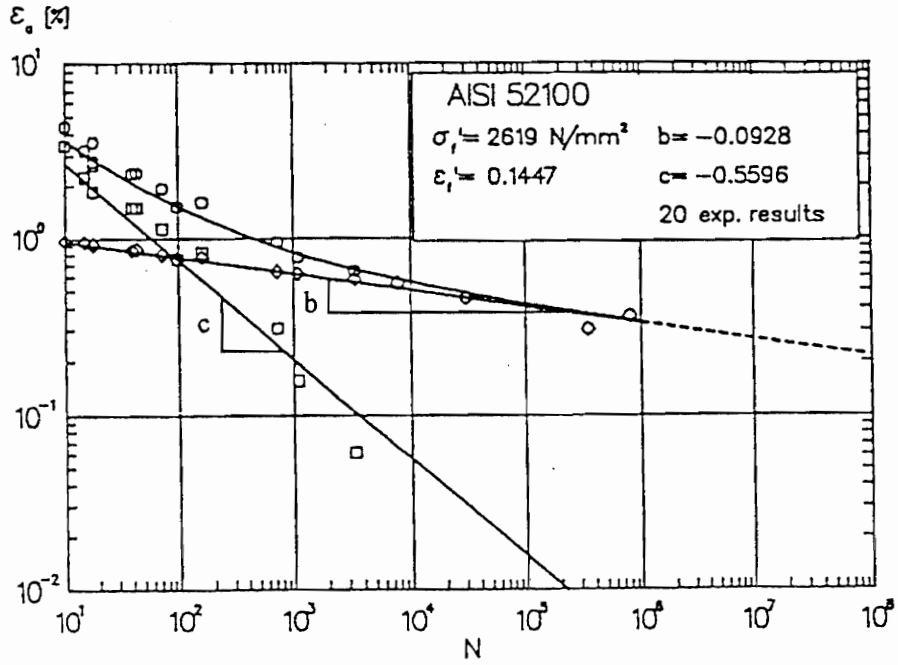


Figure 2-4: Strain - life curve for the steel AISI 52100¹⁴.

In this plot, the total strain resistance is viewed as the sum of the elastic and the plastic strains, and can be characterized by¹³:

$$\frac{\Delta \varepsilon}{2} = \frac{\Delta \varepsilon_e}{2} + \frac{\Delta \varepsilon_p}{2} = \frac{\sigma'_f}{E} (2N_f)^b + \varepsilon'_f (2N_f)^c \quad (2.7)$$

where N_f is the predicted service life,

σ'_f and ε'_f are cyclic properties of the material, and

b and c are the slopes of the two straight lines in the graph.

The elastic and plastic part of this equation are represented by two straight lines in Figure 2-4, the one with a slope b is for the elastic deformation and the other one is for the plastic deformation. The plastic strain is dominant in the low-cycle regime, while at lives greater than about 10^3 cycles, the elastic strain becomes the dominant factor of fatigue. The latter is the case for the cam, which is designed to last several hundred million cycles.

To predict the service life of the cam lobe, several fatigue models^{15,16,17,18} are investigated with a view to handling the complexity of multiaxial cyclic stresses. Moreover, a parameter has to be found to represent the combined multiaxial stress state resulting from residual stresses and the

cyclic stresses (mean stress, stress amplitude). Then, a procedure called most damaged plane is used in conjunction with these fatigue models to find where failure is likely to occur for a particular stress state. Service lives are calculated and from the results, conclusions are drawn concerning these different models. The details of the fatigue analysis are developed in Chapter 5.

2.5 Residual stress fields

In this work, the residual stresses created in the cam lobe during grinding are the major concern. These residual stress fields have been evaluated by Courtney¹⁹ in his Master of Science thesis. He accomplished the first two parts of this three-year project :

- generation of a residual stress field by grinding
- measurement of residual stresses and stress gradients

In his work, an extensive study of the grinding protocol was done in collaboration with Litton Landis. Several cam lobes were ground under various conditions, covering a broad range of grinding protocols. The number of passes and the depth of cut per grinding pass were varied for each lobe in order to have grindings from abusive to gentle. As a result the residual stress profiles created in the cam lobes were also quite different. Then, a limit was set to characterize a lobe as “burned” or “unburned”, where burn is defined as a localized tempering of the cam lobe due to the grinding operation. Burned lobes received an abusive grinding (high depth of cut per grinding pass) and show high residual tensile stresses subsurface, while unburned were ground under gentle conditions and have compressive residual stresses below the surface. He ended his work by characterizing non-destructive evaluating techniques to identify the presence of burn in a lobe, such as the x-ray diffraction line broadening.

To determine the residual stress fields in each lobe, the x-ray technique was used. Stress fields were found in different locations of the cam (nose, ramp, base circle) at various depths, as shown in Figure 2-5. The residual stress data were obtained in three directions along the camshaft (axial, circumferential and normal), as illustrated by Figure 2-6, and put in the format of stress tensors or graphs where residual stress is plotted versus depth at a certain location and direction around the cam, as can be seen in Figure 2-7.

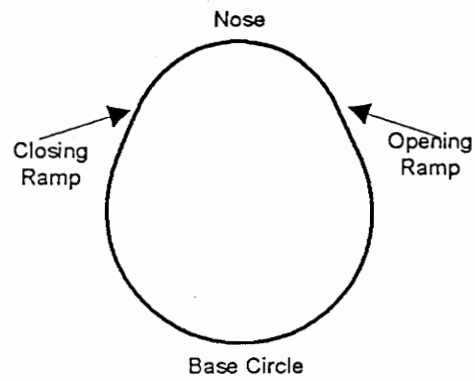


Figure 2-5: Lobe nomenclature(0° :nose, 60° :opening ramp, 180° :base circle, 300° :closing ramp) [Courtney].

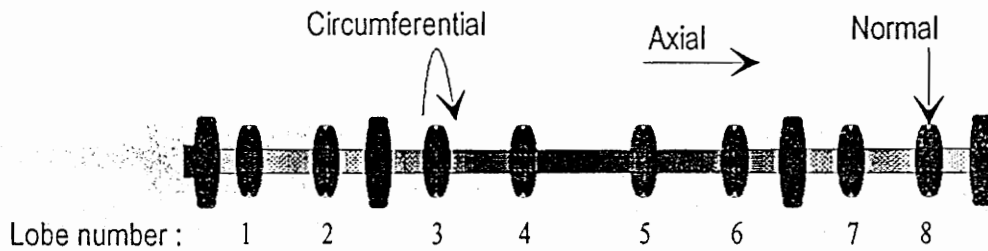


Figure 2-6: Different directions of measurement along camshaft [Courtney].

Analyzing these data, some assumptions are made concerning these residual stresses, and a certain number of lobes are chosen to work with. Additional information about the residual stresses is presented in Chapter 3.

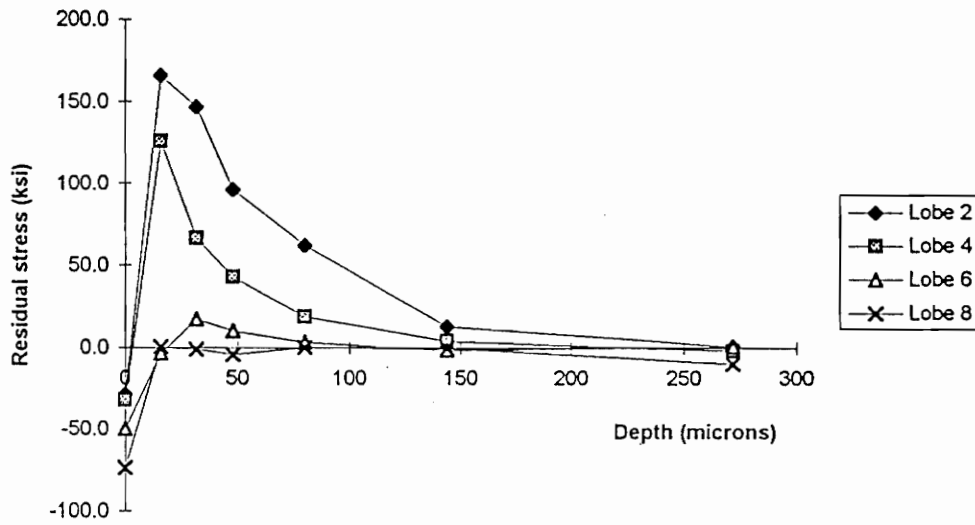


Figure 2-7: Axial residual stresses vs. depth on the base circle for several lobes [Courtney].

The residual stresses are added to the stresses from the contact analysis, to characterize the actual stress field in the lobe. Using this combined stress field, realistic service life predictions are found²⁰, as described in Chapter 5.

3. STRESS ANALYSIS

3.1 Contact Stresses - Case of Two Parallel Cylinders

3.1.1 Area of contact and pressure distribution

The problem of the cam and roller follower is simplified by assuming two parallel cylinders in contact, as shown on Figure 3-1, for the Hertzian analysis. This way, the problem is easier to deal with, but still close to reality and all the results are applicable to the case of the cam and roller follower. This assumption is valid for the roller follower, which is a short cylinder. But, for the cam lobe which has a peculiar shape, different cylinder radii are considered depending on the location: that is, the nose, the base circle and the ramp, as shown on Figure 2-5.

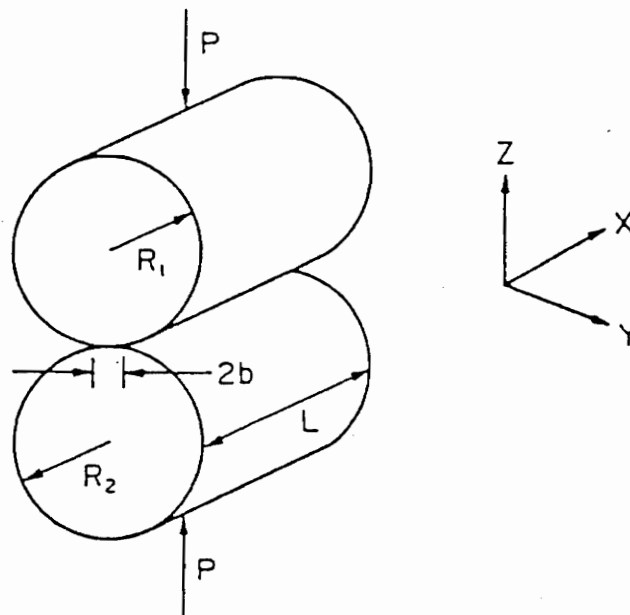


Figure 3-1: Contacting parallel cylinders [Hearn].

The shape of the contact surface and the pressure at any point on this contact can be computed with the Hertzian theory, as was done for the general case. For two parallel cylinders, the contact area has a rectangular shape of width $2b$ and length L , illustrated by Figure 3-2.

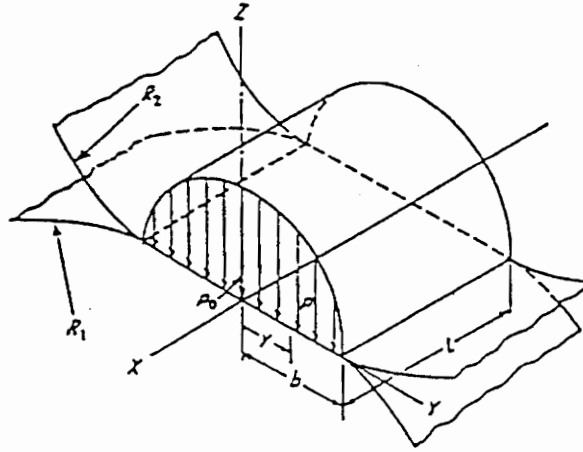


Figure 3-2: Contact pressure distribution [Juvinall].

The value of b , the pressure distribution and the maximum pressure, p_0 are computed. All these data are obtained by knowing the load on these cylinders and the geometric and materials properties, such as Young's modulus, Poisson's ratio, the radius of each cylinder, etc.

The value of b is thus defined by:

$$b = 1.13 \sqrt{\Delta \frac{P}{L \left(\frac{1}{R_1} + \frac{1}{R_2} \right)}} \quad (3.1)$$

where Δ is defined in Equation (2.5).

For the maximum pressure, which is located along the load axis ($y = 0$):

$$p_0 = 0.591 \sqrt{\frac{P \left(\frac{1}{R_1} + \frac{1}{R_2} \right)}{L \Delta}} \quad (3.2)$$

Then, the pressure at any point on the contact area can be defined simply by using y , since the pressure distribution here has a constant section along the x -axis:

$$p = p_0 \sqrt{1 - \frac{y^2}{b^2}} \quad (3.3)$$

If this method is to be used for the case of a flat plate in contact with a cylinder, one of the two radii has to be taken as infinity. This condition is applied on the ramp of the cam.

3.1.2 Limitations of the Hertzian method

As in the general case, the Hertzian method for the particular case of two parallel cylinders has a few limitations. In this theory, the two bodies are assumed to have an elastic and isotropic material behavior. In the case of these two contacting cylinders, there is another very important assumption: the length, L , of the cylinders has to be very large in comparison with their radii, in order to satisfy plane strain conditions. This last assumption is not really fulfilled in this cam and roller-follower system where the length and the radius are of the same order. Therefore, the actual stresses on the border of the cam could be significantly higher than in the center of the contact zone. Thus, plane strain and plane stress conditions should be considered, depending on the location on the cam, as is explained later.

The mechanism used in this work has the following geometric characteristics :

- Radius of the follower : 8.89 mm (0.35 in)
- Radii of the cam on the nose : 12 mm (0.47 in)
on the base circle : 16 mm (0.63 in)
- Length of the cam : 15.8 mm (0.62 in)

3.2 Determination of the contact stresses

3.2.1 Study of two cases

Plane stress and plane strain conditions are now explained, as well as the location where they should be assumed on the cam.

3.2.1.1 Plane stress

A point of the material close to the edge of the cam is assumed to experience plane stress conditions. This means that the normal and shear stresses in the axial direction are zero. The work in plane stress is done in the y-z plane. So, σ_x , τ_{xz} and τ_{xy} are neglected when plane stress conditions are assumed. Although only σ_y , σ_z and τ_{yz} are considered (as illustrated in Figure 3-4), triaxial strains are still used. An example of principal Mohr circles in a plane stress situation is shown on Figure 3-3 (a), where σ_3 is equal to zero.

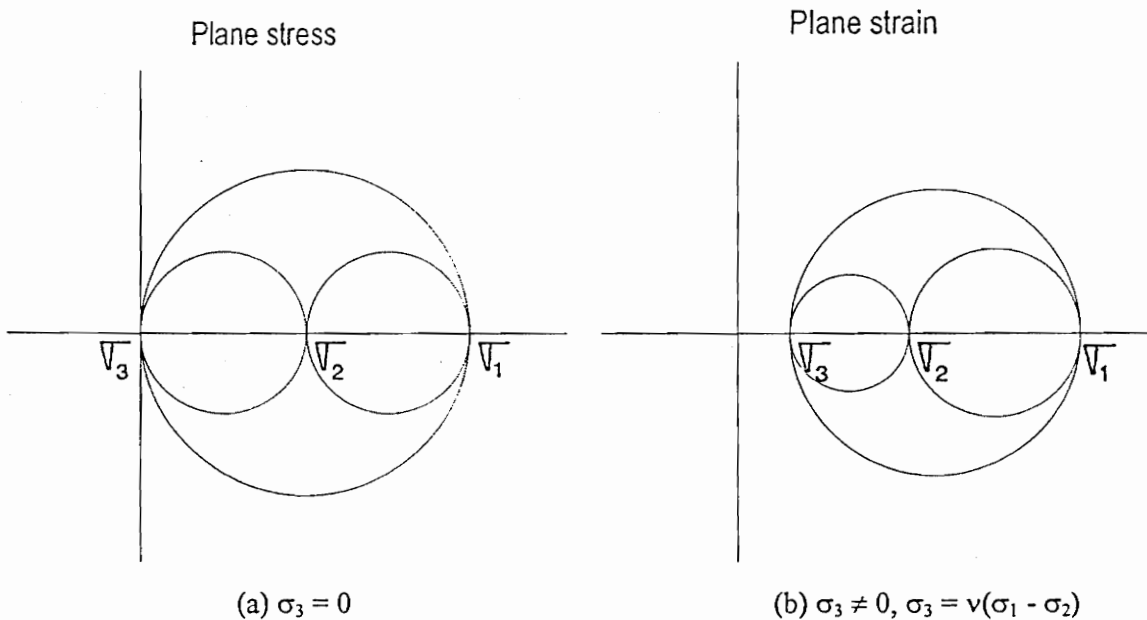


Figure 3-3: Example of Mohr's circle for (a) plane stress and (b) plane strain conditions.

3.2.1.2 Plane strain

A point in the middle of the body in the axial direction (x-axis) is assumed to be in plane strain conditions. In this case, the normal and shear strains in the axial direction are neglected. This means, ϵ_x , γ_{xy} and γ_{xz} will be canceled, but triaxial stresses are still considered. An example of Mohr's circle for a plane stress situation is shown on Figure 3-3 (b), where the three principal stresses are considered.

Differentiating between these two cases is important when the maximum shear stress, which is the radius of the largest circle, needs to be computed. In plane stress, one of the three principal stresses is assumed to be equal to zero, and in plane strain, the three principal stresses are considered. Thus the circles are different and, hence, also the maximum shear stress.

3.2.2 Plane stress

The maximum Hertzian pressure, p_0 , and the width of contact (2b) are computed from the Hertzian analysis for any geometry, material and load. Then, according to Smith and Liu², the plane stresses in the y-z plane, shown in Figure 3-4, can be calculated.

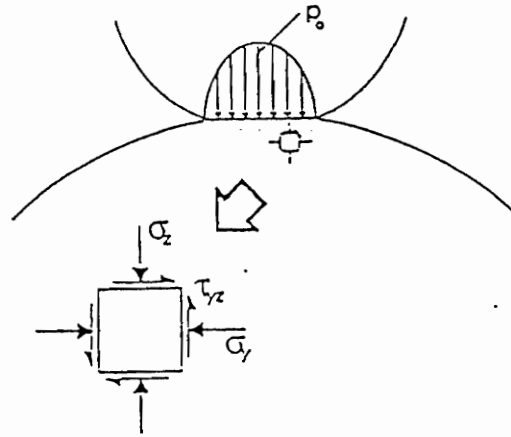


Figure 3-4: Plane stresses in the y-z plane.

3.2.2.1 Stresses in depth

With reference to Figure 3-2, on the surface ($z = 0$) at the load axis ($y = 0$), the plane stresses have the following values:

$$\sigma_y = -p_0 \quad (3.4)$$

$$\sigma_z = -p_0 \quad (3.5)$$

$$\tau_{yz} = 0 \quad (3.6)$$

Subsurface stress field can also be determined over the entire contact area. In this problem, pure rolling contact (no sliding) is assumed between the cam and the follower. All the loads are transmitted in the normal direction to the cam, no tangential loads are considered in the analysis. The method of Smith and Liu² is used in conjunction with this assumption to compute the plane stresses as a function of y , z , p_0 and b :

$$\sigma_y = -\frac{p_0}{\pi} z \left(\frac{b^2 + 2y^2 + 2z^2}{b} \Psi - \frac{2\pi}{b} - 3y\psi \right) \quad (3.7)$$

$$\sigma_z = -\frac{p_0}{\pi} z (b\Psi - y\psi) \quad (3.8)$$

$$\tau_{yz} = -\frac{p_0}{\pi} z^2 \psi \quad (3.9)$$

where Ψ and ψ are:

$$\psi = \frac{\pi}{K_1} \frac{1 - \sqrt{\frac{K_2}{K_1}}}{\sqrt{\frac{K_2}{K_1}} \sqrt{2\sqrt{\frac{K_2}{K_1}} + \frac{(K_1 + K_2 - 4b^2)}{K_1}}} \quad (3.10)$$

$$\Psi = \frac{\pi}{K_1} \frac{1 + \sqrt{\frac{K_2}{K_1}}}{\sqrt{\frac{K_2}{K_1}} \sqrt{2\sqrt{\frac{K_2}{K_1}} + \frac{(K_1 + K_2 - 4b^2)}{K_1}}} \quad (3.11)$$

and where K_1 and K_2 are defined as:

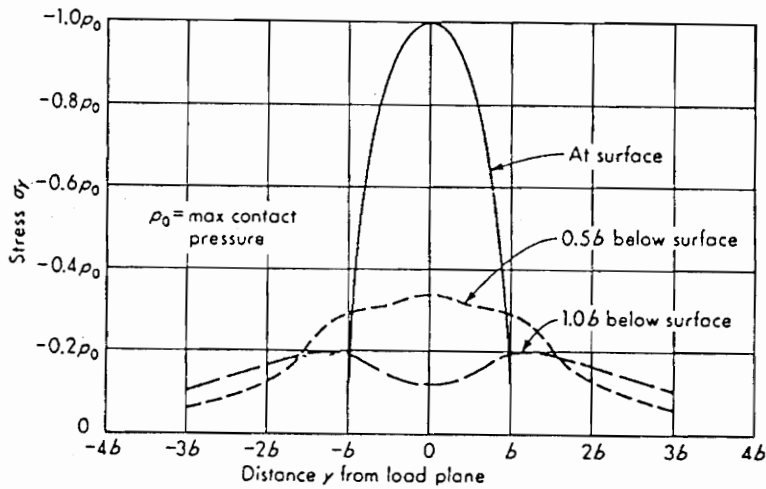
$$K_1 = (b + y)^2 + z^2 \quad (3.12)$$

$$K_2 = (b - y)^2 + z^2 \quad (3.13)$$

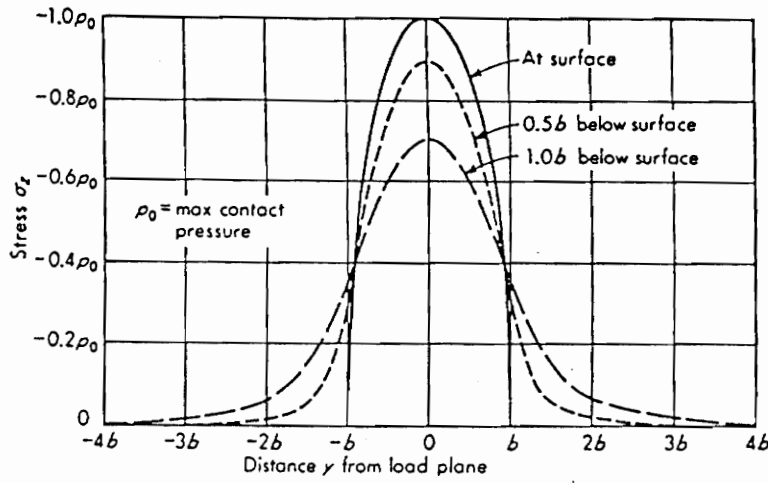
In this way, the plane stresses are determined in depth over the contact region.

3.2.2.2 Maximum values of the different stresses

In Figure 3-5 (a) and (b) are shown the values of the normal plane stresses (σ_y and σ_z) at various points within the contact zone for the case of two parallel cylinders normally loaded. These stress values are given in terms of the maximum Hertzian pressure, p_0 , and the distance along the y-axis is expressed in terms of b (half of the width of contact). From these graphs, a few observations can be made. These normal stresses, σ_y and σ_z , are compressive over the entire contact area. For each depth, their maximum value is on the load axis ($y = 0$). This maximum is equal to $-p_0$ on the surface and decreases with increasing depths (z).



(a)



(b)

Figure 3-5: Normal stress (a) in the y-direction and (b) in the z-direction over the contact area at different depths [Juvinall].

The shear stress (τ_{yz}) distribution, shown in Figure 3-6, is more interesting because it is a reversed stress, with a positive value for y negative and a negative one for y positive (see Figure 3-7). On the surface, this stress is zero over the entire contact area. Then, this shear stress increases with depth, eventually reaching a maximum value subsurface, when the depth is $z = 0.5b$, the distance along the circumferential axis is $y = 0.85b$. The magnitude of this maximum is $0.256 p_0$.

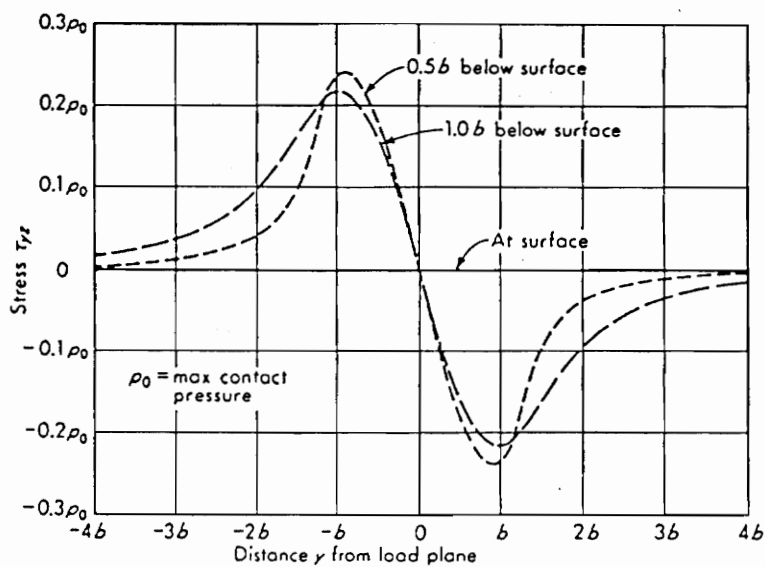


Figure 3-6: Shear stress in the y-z plane over the area of contact at different depths [Juvinall].

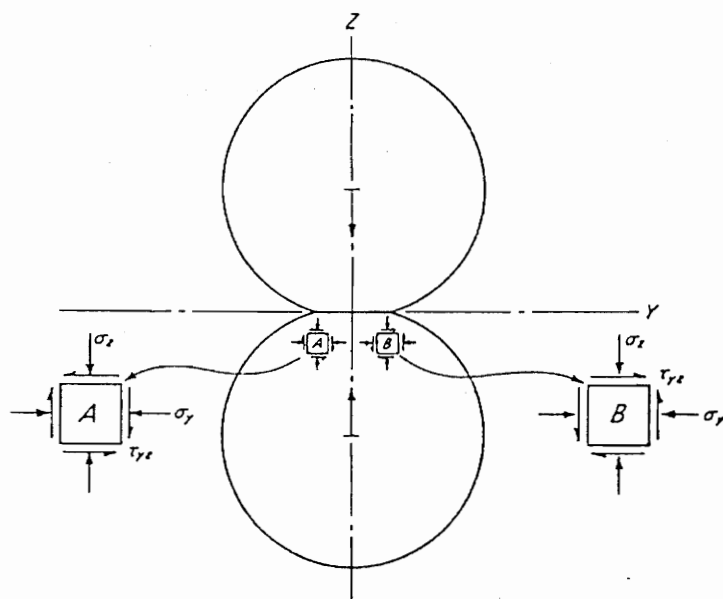


Figure 3-7: Directions of the plane stresses going through the area of contact [Juvinall].

3.2.3 Plane strain

To work in plane strain, the stress in the third direction, σ_x , is computed. This step is simplified by making the assumption that there is no shear stress along the x-axis because it is not in the direction of rolling. Then, the generalized Hooke's law is used, so that σ_x is determined by:

$$\sigma_x = \nu(\sigma_y + \sigma_z) \quad (3.14)$$

Like the two other normal stresses, σ_x is also a compressive stress and has its maximum value on the load axis ($y = 0$). This maximum is $-2\nu p_0$ on the surface, and decreases with increasing depth, as shown on Figure 3-8.

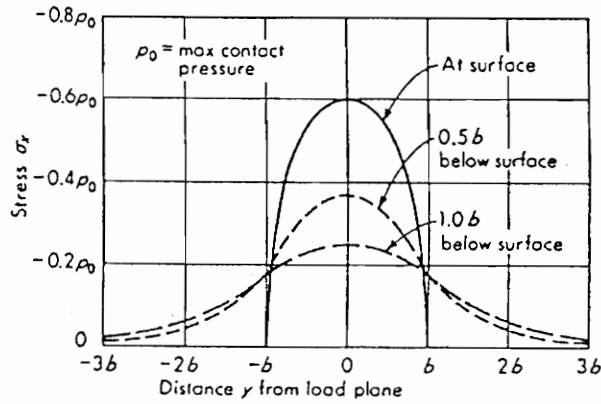


Figure 3-8: Normal stress in the x-direction over the area of contact for different depths [Juvinall].

3.2.4 Principal stresses

Because the complete stress field over the lobe is characterized, it is an easy task to compute the principal stresses. In the axial direction (x-axis), it was assumed that no shear stresses are taking place. So, σ_x is one of the three principal stresses. Concerning the two other principal stresses in the y-z plane, the following formulas are used to compute them:

$$\sigma_1 = \frac{\sigma_y + \sigma_z}{2} + \sqrt{\left(\frac{\sigma_y - \sigma_z}{2}\right)^2 + \tau_{yz}^2} \quad (3.15)$$

$$\sigma_2 = \frac{\sigma_y + \sigma_z}{2} - \sqrt{\left(\frac{\sigma_y - \sigma_z}{2}\right)^2 + \tau_{yz}^2} \quad (3.16)$$

And:

$$\sigma_3 = \sigma_x \quad (3.17)$$

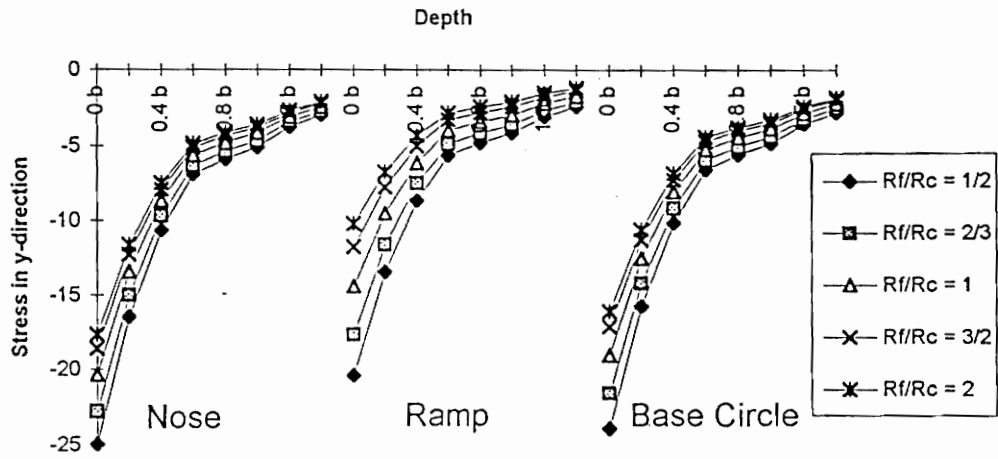
Thus at any point of the body, the principal stresses ($\sigma_1, \sigma_2, \sigma_3$) are known and therefore the principal directions. The maximum shear τ_{\max} , which is needed later in the plasticity criteria and different fatigue models, can be determined from these values.

3.3 Results

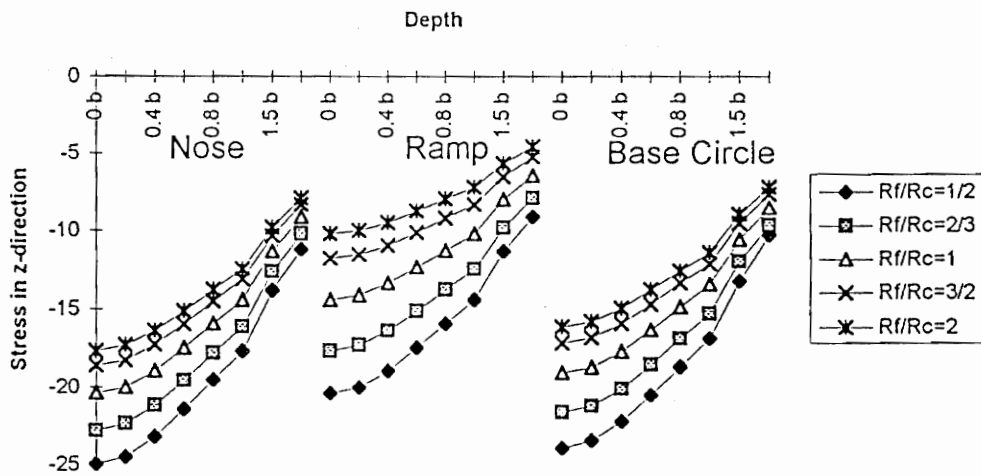
3.3.1 Plane stress

The plane stresses in the y-z plane are first considered. Several ratios of Rf/Rc (radius of the follower over the radius of the cam at the nose) are used to provide some preliminary ideas of these contact stresses where $Rc = 12$ mm. The load is normalized to 1 N in these calculations and results are found for the three plane stresses σ_y , σ_z and τ_{yz} , as illustrated by Figure 3-9 (a) and (b), and Figure 3-10.

On these graphs, the maximum values of the plane stresses are plotted vs. depth for the three locations around the cam : nose, ramp and base circle. As can be seen from these three plots, the maximum values of the normal stresses σ_y and σ_z are always compressive, and decrease with increasing depth. These maximum values have their highest magnitude on the surface, as was shown from the Hertzian analysis combined with Smith and Liu's². Moreover, it is noticed that σ_y decreases faster with the depth than σ_z . In the case of the shear stress, Figure 3-10 shows that its maximum value is positive and attained subsurface around a value of 0.6 b. Actually, this has a significant effect on the fatigue of the body, causing the first cracks to form below the surface.



(a)



(b)

Figure 3-9: Maximum values of the normal stresses (a) σ_y and (b) σ_z vs. depth for different locations around the cam lobe, considering several ratios Rf/Rc ($Rc = 12$ mm).

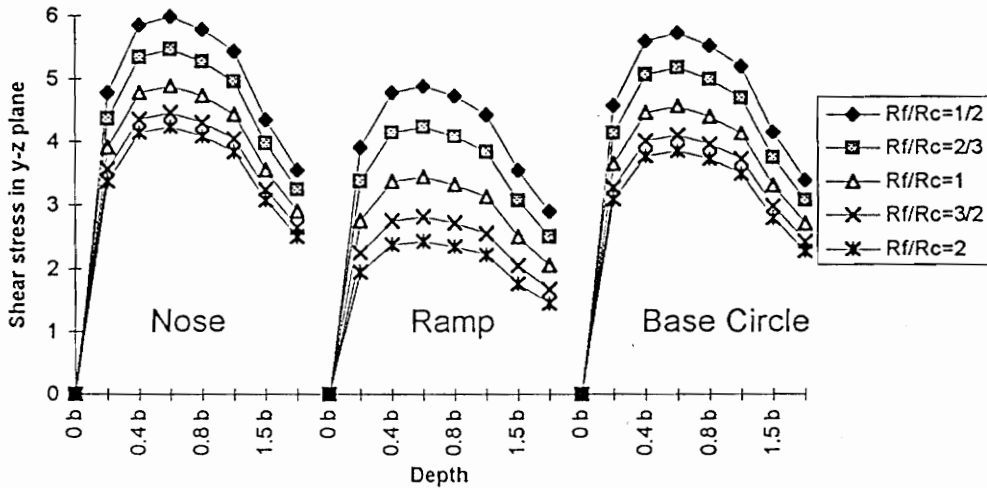


Figure 3-10: Maximum values of τ_{yz} vs. depth for different locations around the cam lobe, considering several ratios R_f/R_c ($R_c = 12\text{mm}$).

The comparison of the stresses between the different ratios R_f/R_c , shows that the smaller the ratio, the higher the stress magnitude. Because same load is distributed on a narrower contact area when one radius is smaller, the stresses are larger. In the present work, the radius of the cam at the nose is 12 mm and the radius of the follower is 8.89mm, giving an R_f/R_c ratio close to 0.75.

After analyzing the maximum values, the variations of these stresses are studied over the entire contact surface. To do this, a point of the material is followed as it enters, proceeds through and exits the area of contact. The complete stress field is then computed in each location this point pass by. A range of computation between $-4b$ and $4b$ along the y-axis is used (as a reminder there is contact between the two bodies only when $-b < y < b$ along this axis). Thus, plots of the three plane stresses before, during and after contact are obtained. In Figure 3-11, these stresses are plotted for the case of the base circle with a maximum Hertzian pressure $p_0 = 220\text{ ksi}$ (1517 MPa) at a depth $z = b/8$, b being 0.14 mm in this case. From these plots, it is demonstrated that the normal stresses σ_y and σ_z are compressive throughout the entire contact zone and their maximum is on the load axis ($y = 0$).

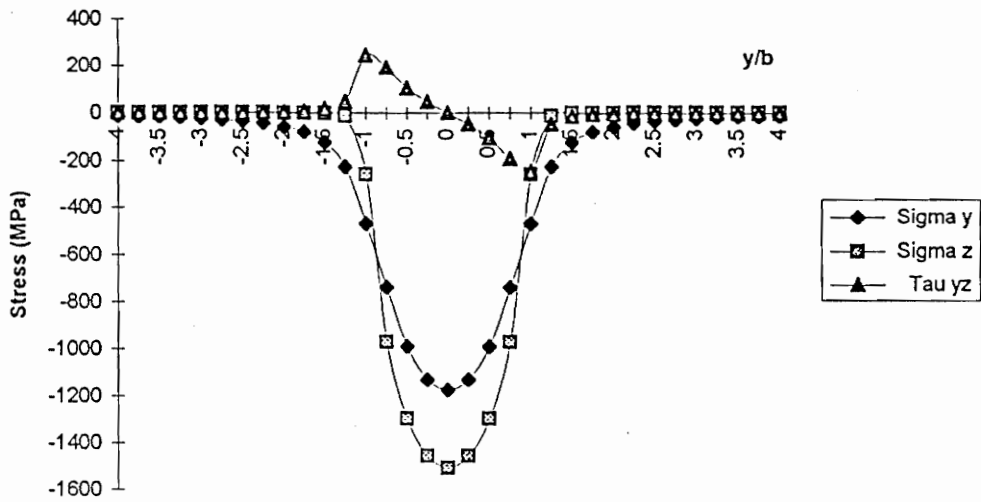


Figure 3-11: Plane stresses over a range $-4b$ to $4b$ along the y -axis at a depth $z = b/8$ on the base circle with $p_0 = 220$ ksi.

The shear stress is observe to reverse sign, changing from positive to negative. The maximum value of this stress is not on the load axis, but around $y = -b$ (actually at $y = -0.85 b$). This value is also reached in compression at the symmetric point, $y = 0.85 b$. On the load axis ($y=0$), the shear stress is zero at all depths and so along the x -axis (axial direction), the normal stresses are equal to the principal stresses.

The plane stresses σ_y , σ_z and τ_{yz} are also studied as a function of depth (along the z -axis) over a range of 0 to b . Figures 3-15, 3-16 and 3-17 are respective 3-D plots of σ_y , σ_z and τ_{yz} on the base circle over a range from $-4b$ to $4b$ along the circumferential direction (y -axis) and 0 to b along the normal direction (z -axis). A p_0 value of 220 ksi (1517 MPa) is used.

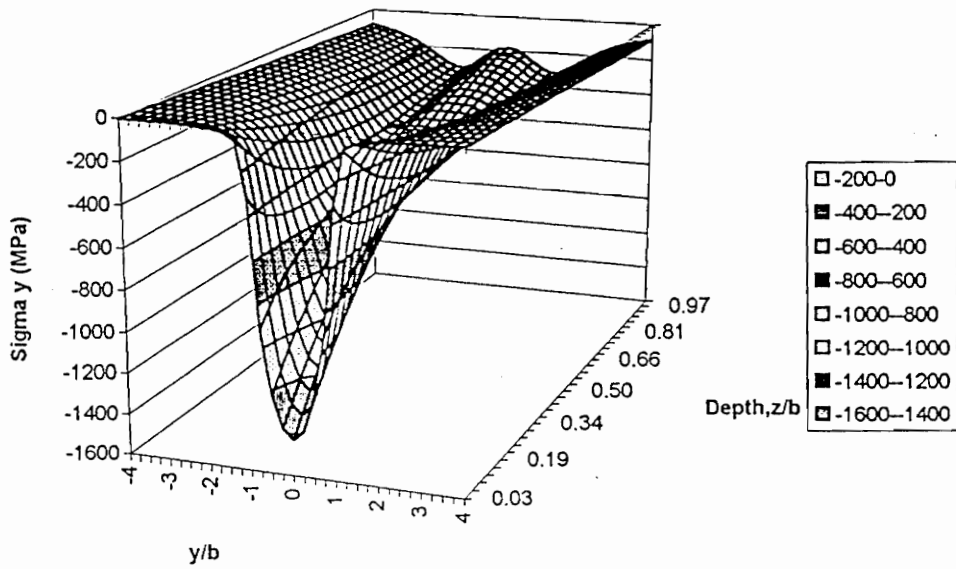


Figure 3-12: 3-D graph of σ_y vs. y and depth on the base circle.

These three graphs corroborate the different points made before. The two normal stresses are always compressive, with a maximum value on the load axis, and decrease with the depth; σ_y decreases faster than σ_z . From Figure 3-14, it is clear that the shear stress is a reversing stress having its maximum value below the surface.

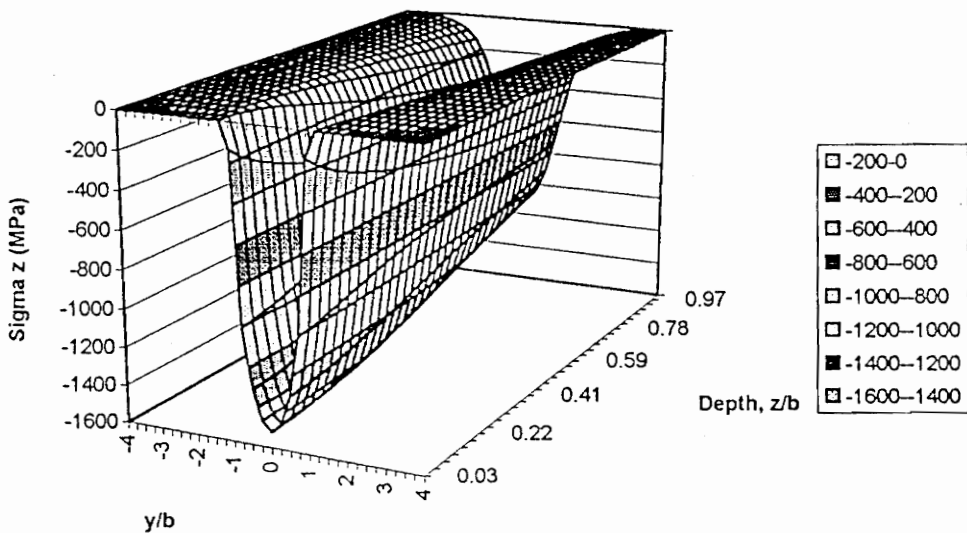


Figure 3-13: 3-D graph of σ_z vs. y and depth on the base circle.

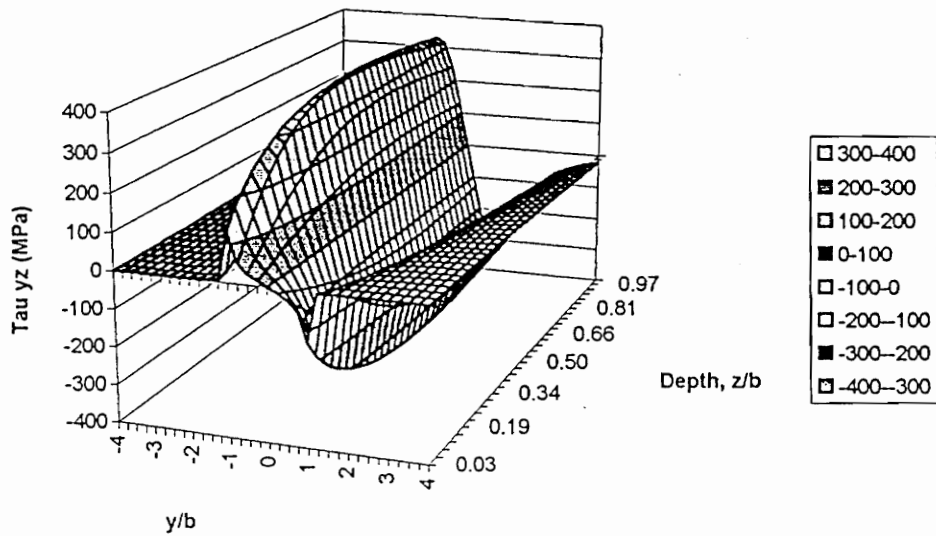


Figure 3-14: 3-D graph of τ_{yz} vs. y and depth on the base circle.

Next to evaluate plane strain conditions, σ_x has to be evaluated in addition to the characterization of these plane stresses.

3.3.2 Plane strain

The general Hooke's law is used to compute this third stress in the x -direction, according to Equation (3.14). Thus, following the example used in the previous section, a 3-D plot of σ_x is obtained, as shown in Figure 3-15.

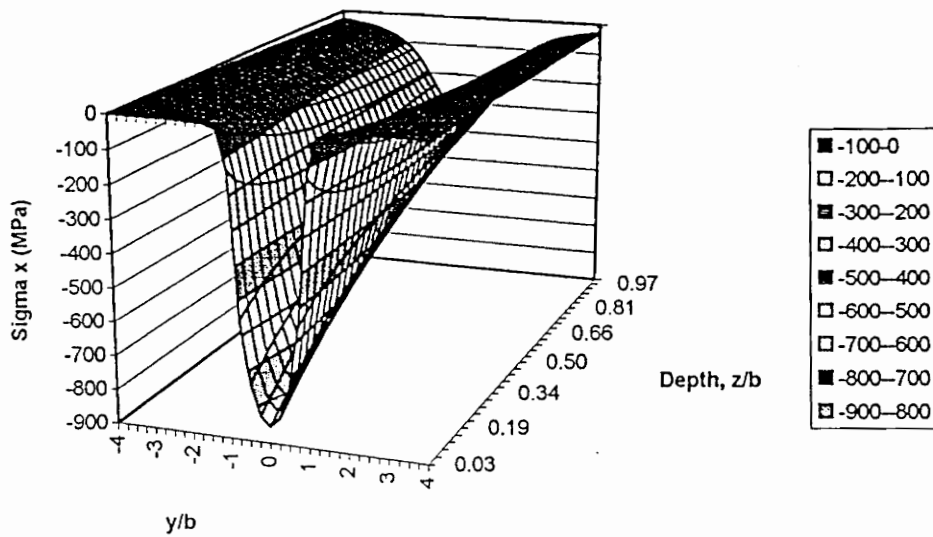


Figure 3-15: 3-D plot of σ_x vs. y and depth on the base circle.

The stress state and distribution of σ_x is similar to σ_y and σ_z in that it is always compressive and has its maximum value on the load axis. However, this maximum has only a magnitude of $-2vp_0$ on the surface, while a value of $-p_0$ was obtained for σ_y and σ_z . Then, the principal stresses magnitude and direction are determined over the contact area.

3.3.3 Principal stresses

These stresses are found using Equation (3.15), (3.16) and (3.17). Then, their orientation and magnitude throughout the entire contact area are computed. The stress, σ_3 , which is equal to σ_x , is always oriented along the axial direction (x-axis).

For the two other principal stresses, their orientation are calculated using the following equation :

$$\tan(2\theta) = \frac{\sigma_y - \sigma_z}{2\tau_{xy}} \quad (3.18)$$

where θ is the angle between the direction of the maximum principal stress and the direction of the maximum normal stress, y-axis or z-axis. Then the direction of the second principal is found just by adding 90° to θ . In Figure 3-16, these principal directions are given at a point which is followed

through the area of contact. On this figure, there is only the part of the rotation for the negative values of y , a mirror image can be obtained once the load axis is crossed ($y > 0$). The magnitude of the principal stresses are given with respect to the maximum Hertzian pressure, p_0 .

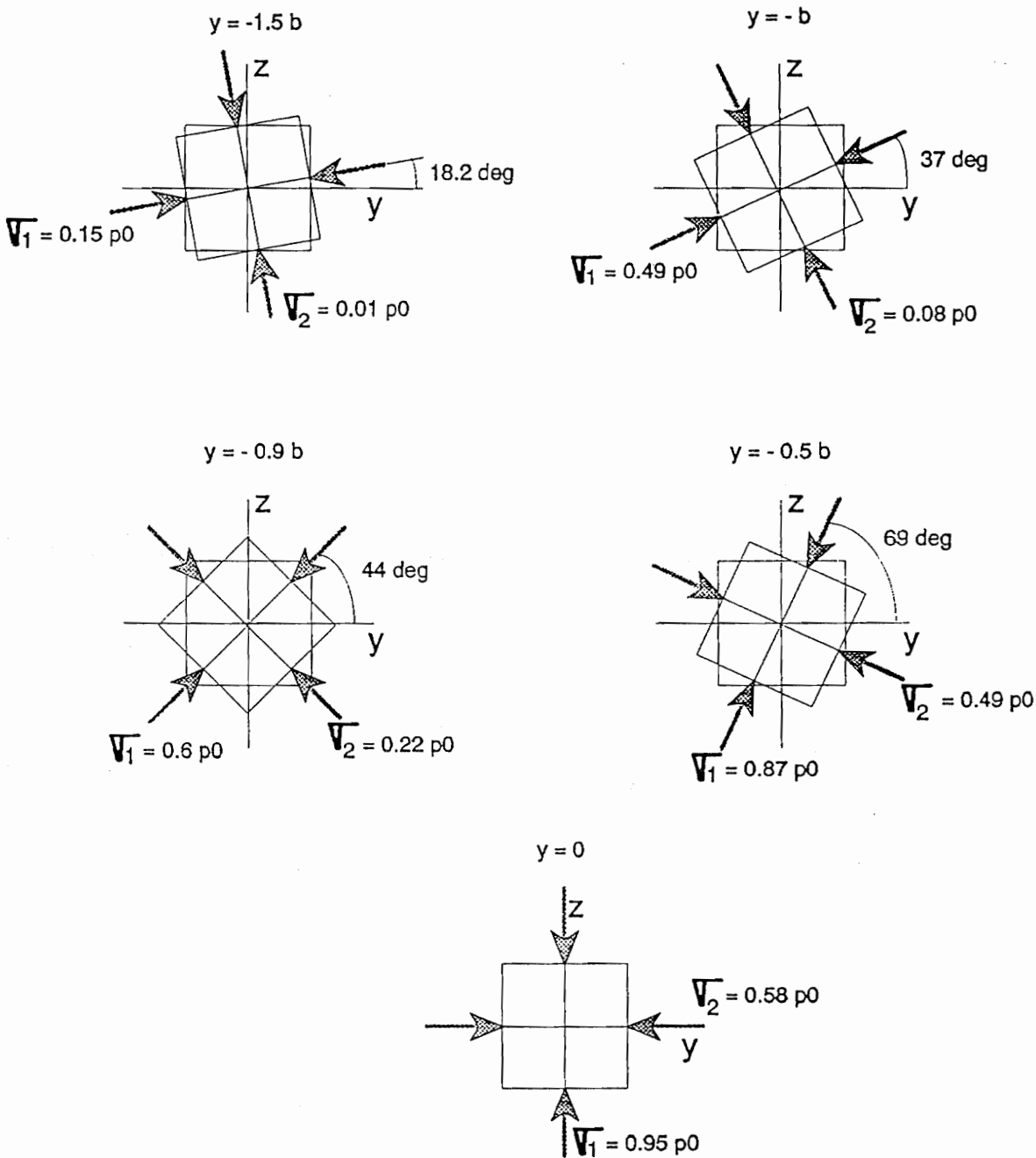


Figure 3-16: Example of the rotation of the principal directions at a depth $b/4$ over the first part of a cycle ($-1.5b < y < 0$).

The rotation of the principal stresses, from this diagram, is 90° over half of the area of contact, so their rotation is 180° over the entire contact surface. Their magnitude is increasing as they get closer to the load axis, eventually reaching a maximum on the load axis ($y=0$) where they are equal to the normal stresses σ_y and σ_z .

3.4 Residual stresses (RS)

Up to this point, only the contact stresses have been considered in this stress analysis. However, the residual stresses characterized in the first part of this project need to be combined with the contact stresses to determine the actual stress field in the cam lobe. These residual stresses are obtained from Courtney's studies¹⁹, where they were characterized experimentally as functions of the location, the direction and the depth (See section 2.5). These stresses are presented in several formats: residual stress tensors, as shown on Table 3-1, graphs of residual stress as a function of depth, as can be seen in Figure 2-7, residual stress at the surface as function of the location around the cam lobe, as illustrated in Figure 3-17.

In Table 3-1, residual stress tensors are shown where the stresses on the diagonal are the normal ones : circumferential, axial and normal directions respectively; and the other components are the shear stresses.

Table 3-1: Residual stress tensors on the base circle for several lobes [Courtney].

lobe 1	lobe 2	lobe 3	lobe 4
$\begin{bmatrix} 13 & 4 & 1 \\ & -14 & 1 \\ & & -4 \end{bmatrix}$	$\begin{bmatrix} 22 & 5 & 2 \\ & 1 & 2 \\ & & 1 \end{bmatrix}$	$\begin{bmatrix} 15 & -1 & 2 \\ & -8 & 1 \\ & & -3 \end{bmatrix}$	$\begin{bmatrix} 23 & 5 & 2 \\ & -7 & 2 \\ & & 0 \end{bmatrix}$
lobe 5	lobe 6	lobe 7	lobe 8
$\begin{bmatrix} 26 & 2 & 3 \\ & 0 & 1 \\ & & 0 \end{bmatrix}$	$\begin{bmatrix} 22 & 7 & 2 \\ & -4 & 1 \\ & & -1 \end{bmatrix}$	$\begin{bmatrix} 23 & 0 & 2 \\ & -6 & 2 \\ & & -5 \end{bmatrix}$	$\begin{bmatrix} 10 & 12 & 1 \\ & -14 & 1 \\ & & -3 \end{bmatrix}$

By analyzing these data, two assumptions are made for the residual stress fields :

- Neglect the residual stresses in the normal direction (z-axis)
- Neglect the residual shear stresses

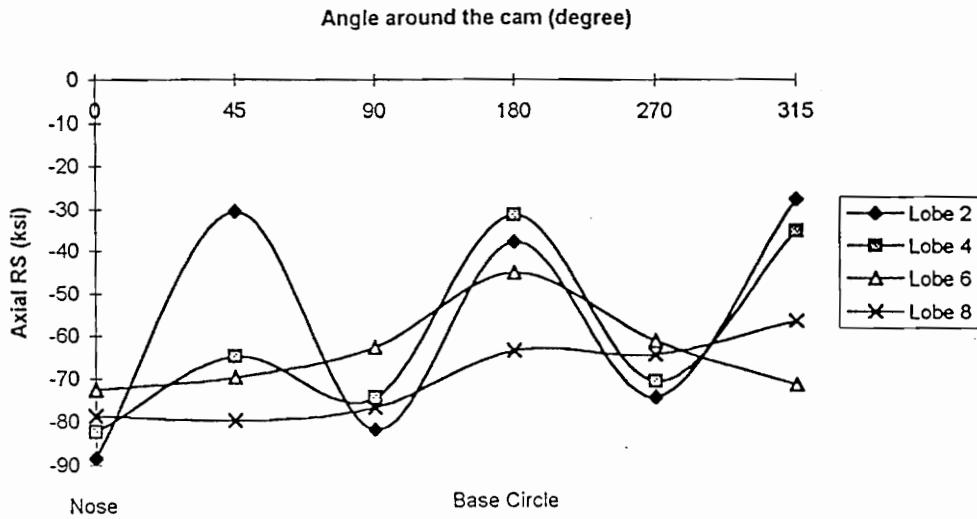


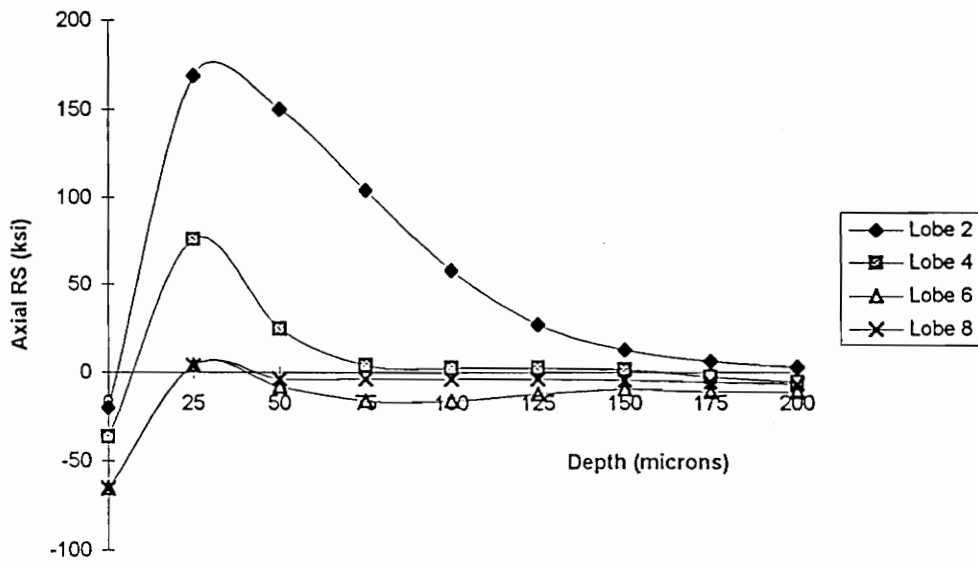
Figure 3-17: Surface residual stress around cam (0°: nose, 60°: opening ramp, 180°: base circle, 300°: closing ramp) in the axial direction [Courtney].

Initially, analyses are developed for two lobes, a “burned” and an “unburned” one; lobe 2 and 8 are chosen for this part. Then, the work is enlarged to two other lobes, 4 and 6, to find a better correlation between the residual stress fields and the service life. Lobe 2 and lobe 8 will be referred to as burned and unburned lobe respectively, later in this study. All these lobes have been ground under different conditions, which have a large effect on their respective residual stress fields. These grinding conditions are summarized in Table 3-2.

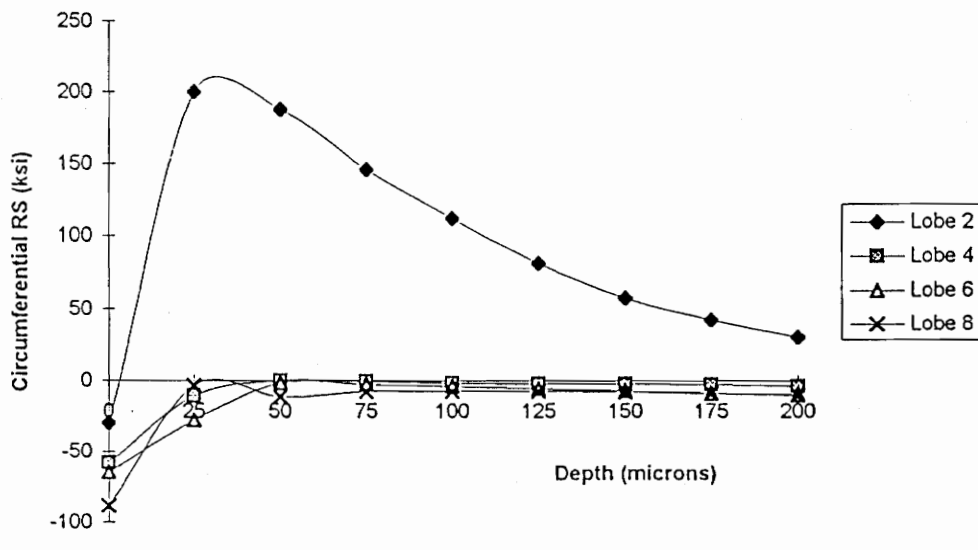
Table 3-2: Number of grinding passes and depth of cut per grinding pass [Courtney].

Lobe number	Number of grinding passes	Depth of cut by pass (mm)
2 (burned)	5	0.09
4	7	0.07
6	10	0.05
8 (unburned)	16	0.03

In this study, the residual stresses are used in the axial and circumferential directions. Their value at a particular depth is found from plots such as Figure 3-18 (a) and (b).



(a)



(b)

Figure 3-18: Residual stress in the (a) axial and (b) circumferential direction on the ramp for several lobes [Courtney].

The cam lobe is divided into three parts, in the present work (See Figure 2-5):

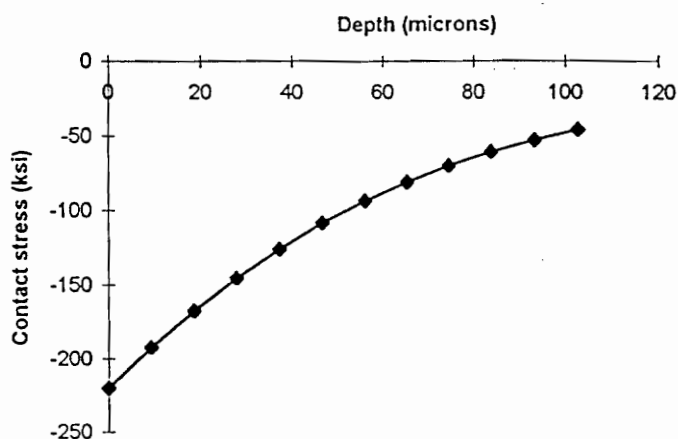
- Nose
- Ramp
- Base circle (BC)

In the preceding graphs, only the case of the ramp is illustrated. The two other locations are detailed in Appendix B. An accurate analysis of all the residual stress data available leads to the following conclusions:

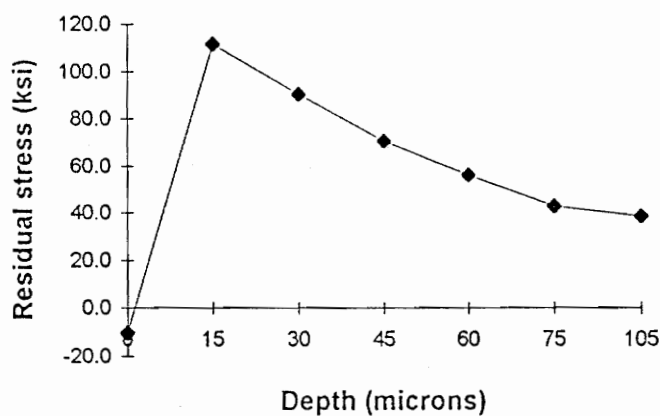
- Lobe 2 (burned lobe) has high tensile subsurface residual stresses on the ramp and on the base circle. On the nose, the residual stress field is less important, but still tensile, due to the dynamic loads applied during grinding by the wheel.
- Lobe 4 has subsurface tensile residual stresses on the lobe and the base circle, but on the nose the residual stress field is compressive.
- Lobe 6 and 8 (unburned lobes) show compressive residual stresses which rapidly decrease to zero, in every location.

3.4.1 Actual stress field

The actual stresses can be obtained by combining both fields, the contact stress field with the residual stress fields. Figure 3-19 (a) and (b) illustrate these two stress fields versus depth on the base circle.



(a)



(b)

Figure 3-19: (a) Contact stress and (b) residual stress fields on the base circle vs. depth.

Once these two fields are summed, the actual stress field is characterized, as it is shown on Figure 3-20 (a) and (b), for the case of the base circle of the burned and the unburned lobes, with $p_0 = 220$ ksi (1517 MPa).

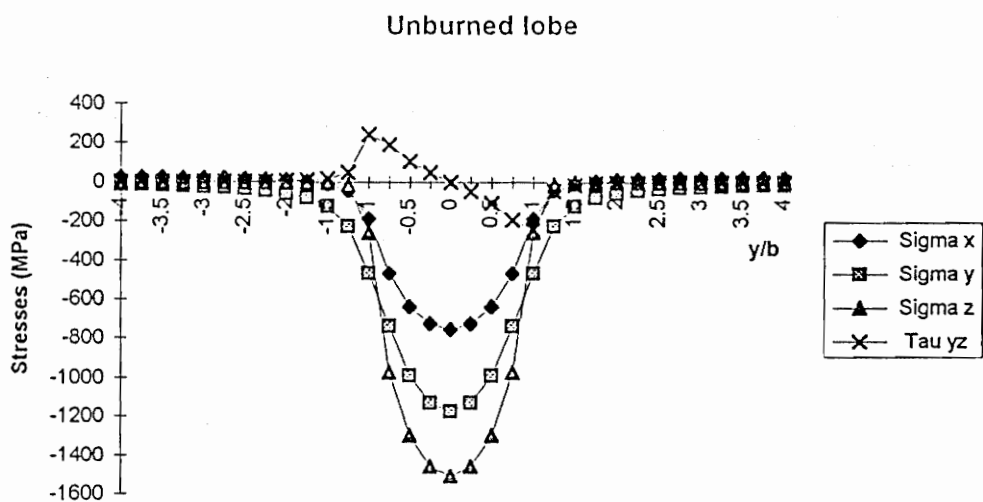
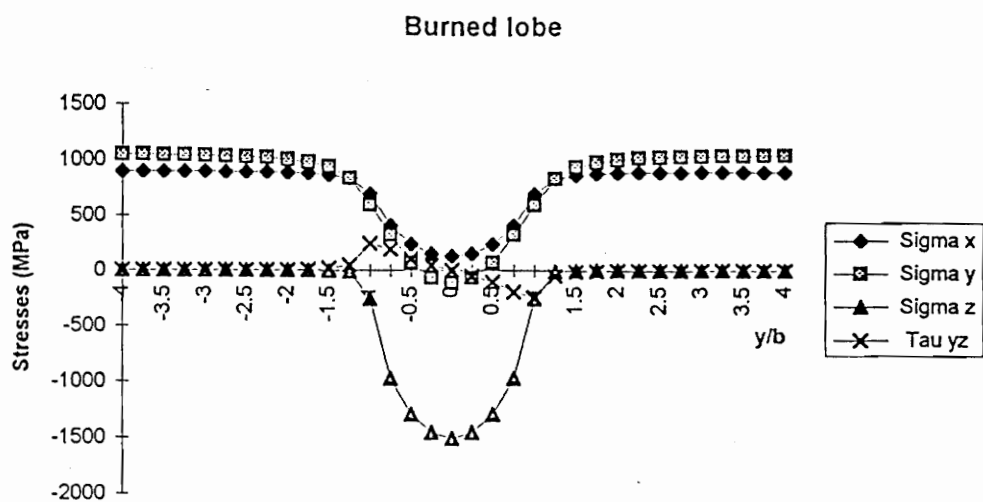


Figure 3-20: Actual stress fields over a range $-4b$ to $4b$ along the y -axis at a depth $z = b/8$ for the base circle of (a) the burned and (b) the unburned lobes.

Comparing these two figures with Figure 3-11 (σ_x does not appear on this figure), it can be seen that :

- σ_z and τ_{yz} are not affected by the summation of the residual stresses because of the assumptions that there were no residual stresses in the normal direction (z-axis) and no residual shear stress was considered.
- On the other hand, σ_x and σ_y are different for each of the two lobes. The high residual stress field in the burned lobe has the effect of shifting σ_x and σ_y almost entirely in the tensile part, as can be seen in Figure 3-20(a). Figure 3-20 (b) demonstrates that there is almost no subsurface residual stresses on the unburned lobe, because σ_y and σ_z are of the same order than when residual stresses are not considered (See Figure 3-11).

The large difference between the contact stress field and the actual stress field, depending on the residual stresses in each cam lobe, can affect the fatigue damage and, hence the service life of this particular lobe, as will be shown later. From these actual stresses, the principal stresses are determined and, because the most damaging stresses are known to be the shear stresses, a study of the maximum shear stress is carried out.

3.4.2 Maximum shear stress

From the principal stresses, the principal shear stresses can be computed :

$$\tau_1 = \frac{|\sigma_2 - \sigma_3|}{2} \quad \tau_2 = \frac{|\sigma_1 - \sigma_3|}{2} \quad \tau_3 = \frac{|\sigma_1 - \sigma_2|}{2} \quad (3.18)$$

The maximum shear stress is then:

$$\tau_{\max} = \text{Max}(\tau_1, \tau_2, \tau_3) \quad (3.19)$$

Continuing to use the example of the base circle with $p_0 = 220$ ksi (1517 MPa), this maximum shear is calculated over a range such as the one used before (-4b to 4b along the y-axis and 0 to b along the z-axis), for the three cases :

- No residual stress
- Burned lobe
- Unburned lobe

The location and magnitude of the highest maximum shear is then isolated and placed in Table 3-3, for the plane strain and plane stress conditions. In this table, the magnitude of the maximum shear stress is normalized with respect to p_0 .

Table 3-3: Location and magnitude of the highest maximum shear stress in the case of the base circle with $p_0 = 220$ ksi.

	Plane Stress		Plane strain	
No residual stress	$y=0 \ z=0$	$\tau_{\max, \text{pl}, \sigma} = 0.5 * p_0$	$y=0 \ z=0.78 * b$	$\tau_{\max, \text{pl}, \epsilon} = 0.3 * p_0$
Burned lobe	$y=0 \ z=0$	$\tau_{\max, \text{pl}, \sigma} = 0.57 * p_0$	$y=0 \ z=0.25 * b$	$\tau_{\max, \text{pl}, \epsilon} = 0.52 * p_0$
Unburned lobe	$y=0 \ z=0$	$\tau_{\max, \text{pl}, \sigma} = 0.67 * p_0$	$y=0 \ z=0.75 * b$	$\tau_{\max, \text{pl}, \epsilon} = 0.3 * p_0$

Once again, it can be seen that the high tensile residual stress field in the burned lobe has a strong effect on the location and magnitude of the maximum shear stress when compared to the case with no residual stress. For the unburned lobe, no such effect can be noticed, only the magnitude in the plane stress case seems to be affected by the residual stresses. This can be explained by the presence of large compressive residual stresses on the surface of this lobe. This table demonstrates that, due to the residual stresses, the actual stress field in each lobe is different. Failure, which is linked to this actual stress state, should then appear in different locations for each cam.

4. PLASTICITY

4.1 Criteria

Because the preceding analysis is based on elastic assumptions, it is next necessary to determine if plasticity occurs during the cyclic loading. Plastic deformation is reached when the stress at a point of the body is greater than the yield strength of the material, monotonic or cyclic. Cyclic loading can change the materials properties, so that yielding can occur at a smaller cyclic yield strength, as shown on Figure 2-2. In the uniaxial case, when the stress, σ , is higher than the uniaxial yield strength, σ_0 , plasticity is present and the body experiences permanent deformation.

The stress problem is more complex in our case, since it is a multiaxial stress problem. Several criteria exist, which can be computed from the multiaxial stress state, to characterize the presence of plasticity. Then, yielding is said to have occurred when this criterion reaches a certain limit, which is defined by a “yield surface” or “yield locus” in the stress plane. Thus, as long as the stress state at a point of the material stays in this “yield locus”, yielding does not occur. The two criteria use for this analysis are the two most common ones :

- Tresca (maximum shear stress) criterion
- von Mises (octahedral shear stress) criterion

Following is a brief description of each of them.

4.1.1 Tresca criterion

This criterion uses the maximum shear stress because the mechanism of yielding is based on the slip of crystal planes which is due to the shear stress. Once the stress state has been determined and principal stresses are known, principal shear stresses (τ_1 , τ_2 and τ_3) can be computed, following the relations given in Equation (3.18).

Then, Tresca criterion is defined by:

$$\tau_{Tresca} = \text{Max}(\tau_1, \tau_2, \tau_3) \quad (4.1)$$

Yielding occurs when this criterion reaches a critical value τ_0 , which is determined using the uniaxial strength σ_0 :

$$\tau_0 = \frac{\sigma_0}{2} \quad (4.2)$$

A useful tool is the effective stress linked to this Tresca criterion, which is:

$$\sigma_{\text{eff.Tresca}} = \text{Max}(|\sigma_1 - \sigma_2|, |\sigma_2 - \sigma_3|, |\sigma_3 - \sigma_1|) \quad (4.3)$$

Then, using this effective stress, yielding is present if the following condition is fulfilled:

$$\sigma_{\text{eff.Tresca}} \geq \sigma_0 \quad (4.4)$$

With each criterion, a “yield locus” can be defined in the stress plane. For Tresca, the yield locus is a hexagon, as shown on Figure 4-1. This “yield locus” permits an easier visualization of the criterion, because when the stress state at a point of the material is outside of this surface there is yielding, otherwise there is only elastic deformation.

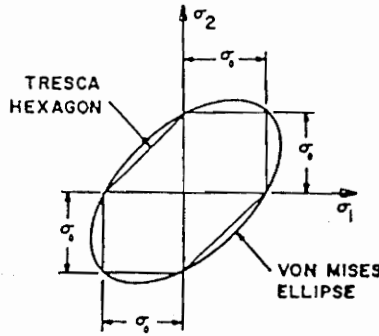


Figure 4-1: Yield surfaces in the two dimensional stress system [Liebowitz].

4.1.2 Von Mises criterion

This criterion is also defined sometimes as the octahedral shear stress criterion. It is based on the octahedral shear stress which occurs on eight different planes and is not very much smaller than the maximum shear stress. This criterion can be defined as follows:

$$\tau_{\text{vonMises}} = \frac{1}{3} \sqrt{(\sigma_1 - \sigma_2)^2 + (\sigma_2 - \sigma_3)^2 + (\sigma_3 - \sigma_1)^2} \quad (4.5)$$

As in the preceding case, yielding occurs when this criterion reaches a critical value τ_{h0} , which can be defined from the uniaxial yield strength σ_0 by:

$$\tau_{h0} = \frac{\sqrt{2}}{3} \sigma_0 \quad (4.6)$$

The effective stress related to this von Mises criterion is:

$$\sigma_{\text{eff.vonMises}} = \frac{1}{\sqrt{2}} \sqrt{(\sigma_1 - \sigma_2)^2 + (\sigma_2 - \sigma_3)^2 + (\sigma_3 - \sigma_1)^2} \quad (4.7)$$

If this effective stress is used, yielding appears when:

$$\sigma_{\text{eff.vonMises}} \geq \sigma_0 \quad (4.9)$$

This second criteria defines a “yield locus” which is an ellipse in the stress plane, shown on Figure 4-1. From this figure, it can be seen that the Tresca hexagon is inscribed in the von Mises ellipse, thus von Mises is more conservative than Tresca.

4.2 Results of the criteria computations

Knowing the principal stresses in any point, computation of the effective stresses is a simple task and can be performed over the entire contact area to determine the maximum value. Three locations around the cam are considered, each at different depths. No calculations are executed on the surface because the residual stress fields are compressive at all locations at this level. Depths varying between $0.2b$ and $0.75b$ are analyzed, because this is the range where the residual stresses are particularly large.

The following 3-D graphs illustrate the computation of Tresca and Von Mises effective stresses at a depth $z = 0.2b$ and $z = 0.75b$ over a range of p_0 between 200 ksi and 300 ksi. These effective stresses are studied for the burned and unburned lobes on the nose (N), ramp (R) and base circle (BC), as well as when no residual stresses (No RS) are present. It is important to recall that the burned lobe shows some high subsurface tensile residual stresses, and the unburned one only shows some compressive residual stress fields below the surface. Both monotonic and cyclic yielding limits appear, because the cam could be subject to either initial yielding or cyclic yielding. For the steel used, AISI 52100, in this work, the yielding limit are :

- monotonic yielding = 1924 MPa
- cyclic yielding = 1339 MPa

These two limits are on the 3-D graphs, so that a direct comparison could be made between the effective stress and the yield strength.

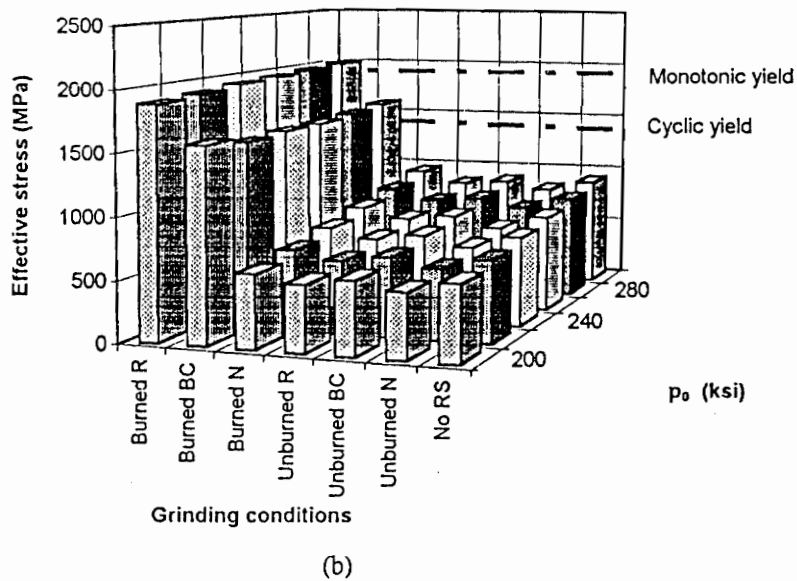
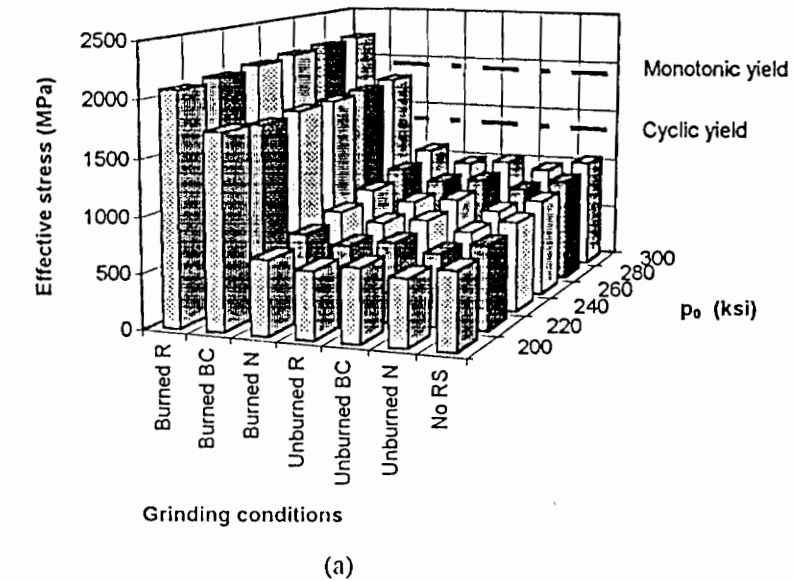
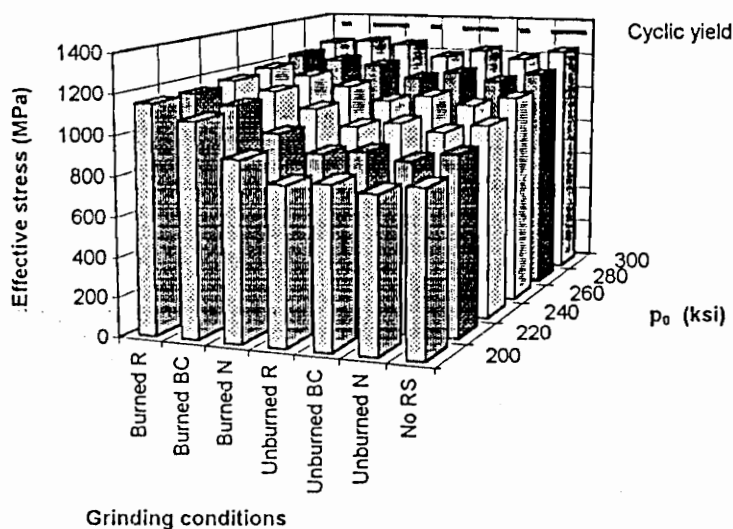


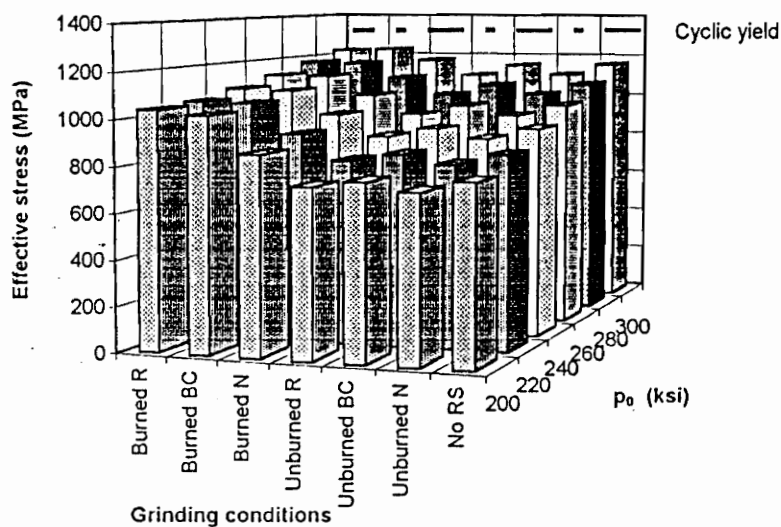
Figure 4-2: (a) Effective Tresca stress and (b) effective von Mises stress over a range of maximum Hertzian pressure from 200 ksi to 300 ksi at a depth of $0.2b$ for several cases.

Figure 4-2 (a) and (b) illustrate the case of Tresca and von Mises respectively, at a depth $z = 0.2b$, which is close to the surface. From these two graphs, the von Mises effective stress is always smaller than Tresca effective stress; it is more conservative. This will also be noticeable in the fatigue life predictions. At this depth, the tensile residual stresses for the burned lobe on the ramp

and base circle, are predominant, so the effective stress is quite large. The difference between these two locations and all the other cases is enormous. For the unburned lobe, the effective stress is always smaller than the case without residual stresses, which is explained by subsurface residual compressive stresses on this lobe.



(a)



(b)

Figure 4-3: Effective (a) Tresca and (b) von Mises stresses over a range of maximum Hertzian pressure from 200 ksi to 300 ksi at a depth of $0.75b$ for several cases.

The case of a depth $z = 0.75b$ is shown in Figure 4-3 (a) and (b). At this level below the surface, differences between lobe locations grow smaller since the residual stress fields are attenuated. The dominant stresses are the contact stresses at this depth.

The four preceding 3-D plots show that the monotonic and cyclic yielding strengths are exceeded only at a depth close to the surface, $z = 0.2b$. The effective stress, Tresca or von Mises, is larger than these yielding limits on the ramp and the base circle of the burned lobe. But only on the ramp, is the effective stress larger than the monotonic yielding strength. Thus, at this location there might be an initial plasticity followed by a possible cyclic softening. The deformation should be readjusted in the elastic range after a short time, as will be shown in the next section. For the depth $z = 0.75b$, the effective stress does not exceed in any case one of the yielding limits. So, no radical change in the residual stresses should take place at this depth.

4.3 Stress relaxation

The preceding analysis concluded that yielding and cyclic softening could occur on some locations of the burned lobe at certain depths close to the surface. This concerned only the ramp and the base circle of this lobe. All the others cases did not show any yielding.

It is important to notice the two following points :

- A camshaft is made to last several hundred millions cycles and at such a long life regime, elastic deformation is the predominant part of fatigue, as was explained earlier.
- The residual stress fields, in Courtney's work, had been characterized just after the grinding operation. If these camshafts were put in an engine, run for a certain amount of time and the residual stresses measured again, some changes in the magnitudes of these stresses might be noticeable. The magnitude would be expected to decrease, but unfortunately no data are available to verify this.

These two points led to the assumption that a relaxation, a rearrangement of these residual stress fields over the first few cycles, is possible by cyclic softening. To represent this behavior, a relaxation model developed by Landgraf and Chernenkoff²⁰, was used. If a stress cycle, such as Figure 4-4, is considered where the mean stress, σ_m , the maximum and minimum stresses, σ_{max} and σ_{min} respectively and the stress amplitude, σ_a , are known, then there would be relaxation if the magnitude of σ_m decrease with the number of cycles, as illustrated by Figure 2-3.

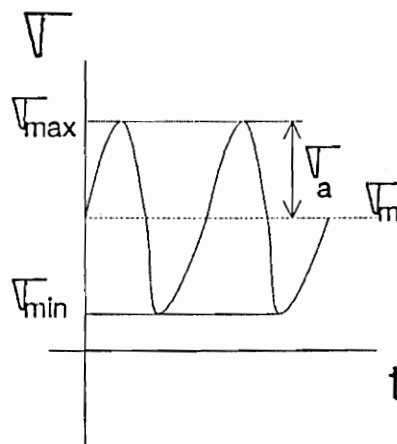


Figure 4-4: Example of a stress cycle.

The relaxed mean stress after N cycles, σ_{mNth} , is computed from the original mean stress, σ_{m1st} , according to the Landgraf and Chernenkoff model :

$$\sigma_{mNth} = \sigma_{m1st} (N)^r \quad (4.10)$$

where r is the stress relaxation rate :

$$r = 8.5 * 10^{-2} \left(1 - \frac{\Delta \varepsilon}{\Delta \varepsilon_{th}} \right) \quad (4.11)$$

and $\Delta \varepsilon$ = applied strain range which can be calculated from the stress range

$\Delta \varepsilon_{th}$ = strain threshold relaxation below which relaxation can not occur

$$\Delta \varepsilon_{th} = 2 \exp[-8.41 + 5.36 * 10^{-3} (HB)] \quad (4.12)$$

where HB = Brinell Hardness

This procedure is used to evaluate the relaxed mean stress as a function of the number of cycles, and to then observe if plasticity would still be present or not. If plasticity disappears after a few hundred cycles, only elastic deformation would be consider for the rest of the analysis.

4.4 Results of the relaxation

The preceding procedure is used to characterize the mean stress relaxation. For this, it is first necessary to compute the stress applied to a particular point of material (depth and location) over one cycle. Thus, the effective Tresca stress is evaluated over an entire cycle, then the values of the mean stress, the maximum and minimum stresses and the stress amplitude are found from graphs such as Figure 4-5. Eventually, they are used in the relaxation model. Following are the effective stresses over one cycle on the base circle of the burned and unburned lobes, still with a maximum Hertzian pressure $p_0 = 220$ ksi.

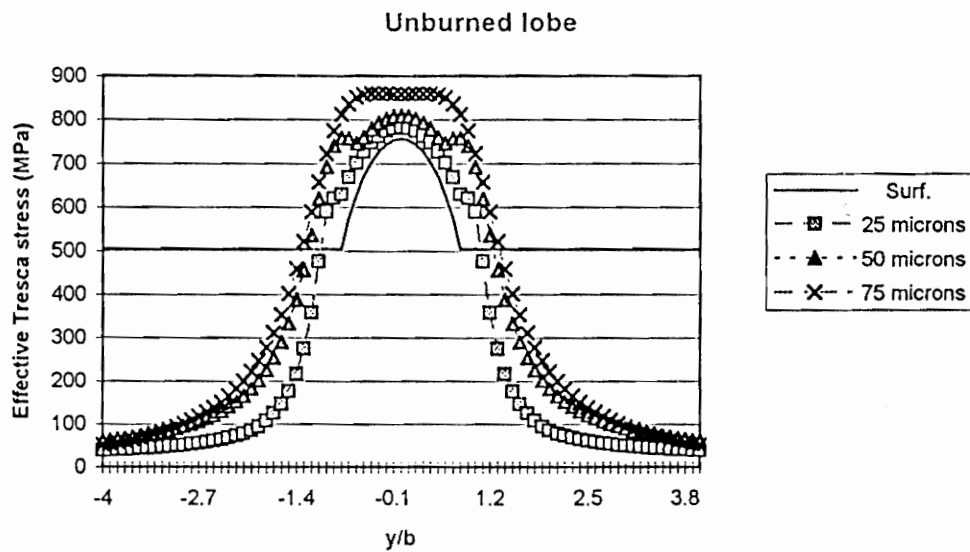
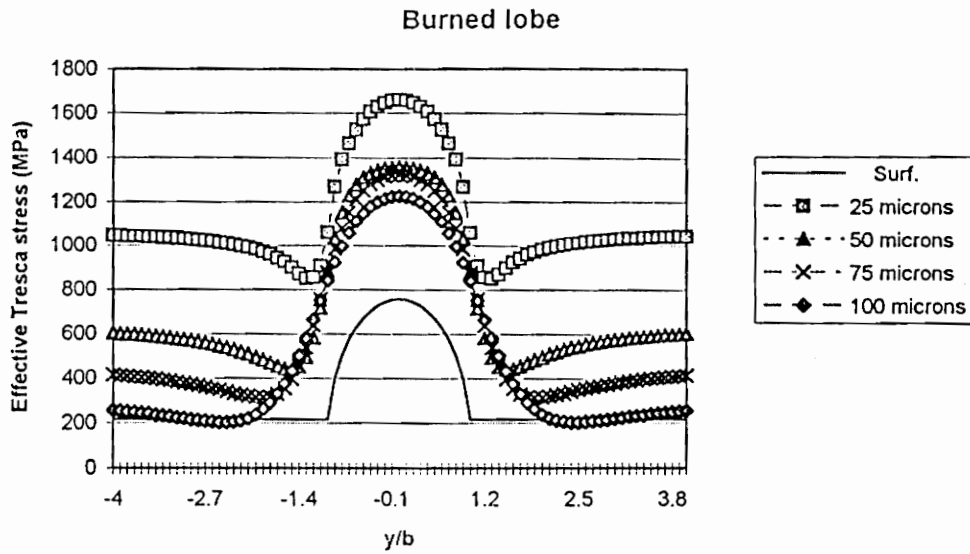
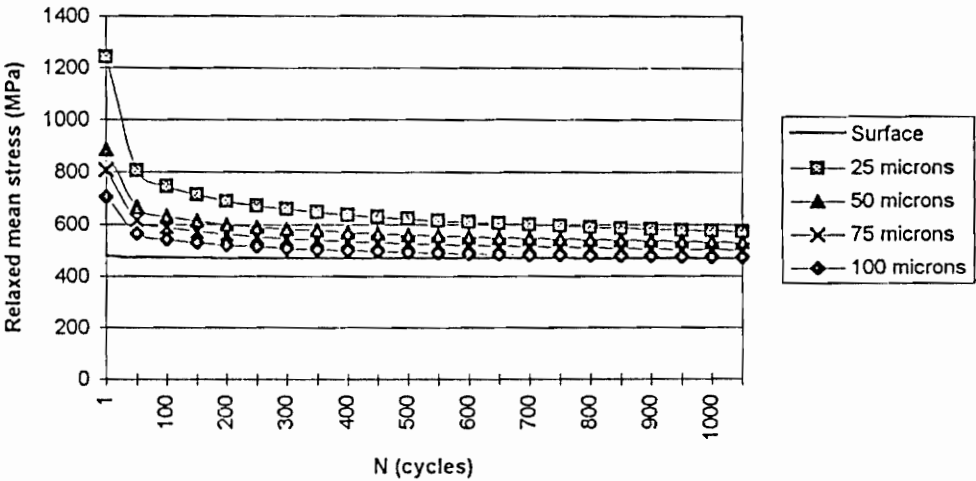


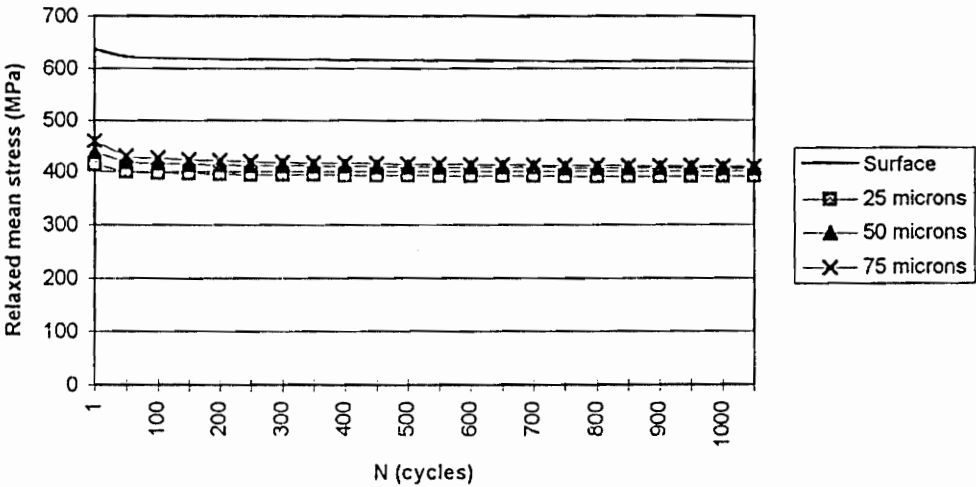
Figure 4-5: Effective Tresca stress on the base circle of the (a) burned and (b) unburned lobes over a range from $-4b$ to $4b$ on the y -axis at different depths.

Figure 4-5 (a) and (b) illustrate stress cycles on the base circle at different depths, including the residual stress fields characterized after grinding. From these figures the strain range, $\Delta\epsilon$, the original mean stress, σ_{m1st} , can be found, as well as the maximum and minimum stresses, σ_{max} and

σ_{min} and the stress amplitude, σ_a . Then, the relaxed mean stress after N cycles, σ_{mNth} , is computed and plotted vs. the number of cycles, as can be seen in Figure 4-6 (a) and (b). The steel used in this work has a Brinell Hardness of 519 HB, so $\Delta\epsilon_{th} = 0.00719$ from Equation (4.12).



(a)



(b)

Figure 4-6: Relaxation of the mean stress on the base circle of the (a) burned and (b) unburned lobes for different depths.

According to this relaxation model, stability is reached after the first 600 hundred cycles. It is noted that this represents the worst case, in that the material is assumed to have achieved cyclic stability. This relaxation takes place subsurface, mainly at the depths close to the surface and is more important on the burned lobe. For example, Figure 4-6 (a) demonstrates that the mean stress at a depth $z = 25$ microns would have its magnitude decreased by 50 % when stability is attained, and by 35 % at a depth $z = 50$ microns. Concerning the unburned lobe, relaxation is far less important, but no yielding was observed on this lobe.

5. LIFE PREDICTIONS

5.1 Fatigue models

The stresses generated by the contact between the cam and the roller follower are determined using an extended Hertzian analysis. This stress state in the cam is characterized in the triaxial stress system at any point of this body, and is shown to be cyclic, due to the rotation of the camshaft. In the fatigue analysis, all these factors have to be considered to obtain valid predictions of the service life of the cam lobe.

The effective stress linked to Tresca and von Mises criteria is considered as an efficient tool to represent the multiaxial stress state at a point through the principal stresses. This effective stress is computed over a cycle at the different locations, so that a cyclic stress diagram is obtained, as was illustrated for the base circle in the preceding section. From this stress cycle, the mean stress, σ_m , the stress amplitude, σ_a , and other stress parameters, such as the maximum and minimum stresses, are determined for use in the fatigue models.

Knowing that this problem involves cyclic multiaxial stress, which can be in terms of an effective stress, correct fatigue models (or parameters) have to be chosen in order to obtain valid service life predictions for this cam lobe.

The models considered for this task are:

- Morrow¹³
- Smith Watson Topper¹³
- Socie¹⁶

These models are in common use and are generally presented in a strain-based form. They are modified and simplified using Hooke's law with the assumption that plastic deformations are negligible. Following is a description of each model.

5.1.1 Morrow model

This model is based on the normal strain particularly on the strain amplitude, ϵ_a , and on the mean stress, σ_m , of the cyclic situation. It is defined by the following relation¹³, derived from Equation (2.7) with a mean stress correction introduced in the elastic term:

$$\epsilon_a = \left(\frac{\sigma'_f - \sigma_m}{E} \right) (2N_f)^b + \epsilon'_f (2N_f)^c \quad (5.1)$$

where N_f = fatigue life,

E = Young's modulus, and

$c, b, \sigma'_f, \epsilon'_f$ = fatigue properties of the material.

The second term of the right hand side of Equation (5.1) which represents the plastic part of the deformation is neglected and Hooke's law is used. The following equation is obtained:

$$\sigma_a = (\sigma'_f - \sigma_m) (2N_f)^b \quad (5.2)$$

The residual stress field is included in the computation of the effective stress. So, Equation (5.3) is used to obtain an expression for the service life, N_f :

$$N_f = \frac{1}{2} \left(\frac{\sigma_a}{\sigma'_f - \sigma_m} \right)^{\frac{1}{b}} \quad (5.3)$$

where σ_m includes the residual stresses.

5.1.2 Smith Watson Topper model (SWT)

For this model, the life of a component, N_f , subject to a cyclic stress situation, is assumed to be a function of the product $\sigma_{\max} \epsilon_a$, where ϵ_a represents the strain amplitude and can be derived from the stress amplitude σ_a , because elastic behavior is assumed. σ_{\max} is naturally the maximum stress. This model is of the form¹³:

$$\sigma_{\max} \epsilon_a = \frac{(\sigma'_f)^2}{E} (2N_f)^{2b} + \sigma'_f \epsilon'_f (2N_f)^{b+c} \quad (5.4)$$

where all the parameters are as defined previously.

The second term of this relation represents the plastic part of the deformation. As it was demonstrated earlier, no plasticity is considered in this work, so this second term is neglected. This assumption combined with Hooke's law simplifies Equation (5.4) to:

$$\sigma_{\max} \sigma_a = (\sigma'_f)^2 (2N_f)^{2b} \quad (5.5)$$

From this expression, the service life, N_f is determined:

$$N_f = \frac{1}{2} \left(\frac{\sqrt{\sigma_{\max} \sigma_a}}{\sigma'_f} \right)^{\frac{1}{b}} \quad (5.6)$$

5.1.3 Socie model

This approach is based on the largest amplitude of the shear strain on the critical plane, so it is of particular interest in the present problem, because the formation of subsurface cracks is assumed to be related to this shear strain, or to the shear stress which is linked to it. This model uses not only the shear strain amplitude, γ_{ac} , but also the maximum normal stress on the maximum shear strain plane, $\sigma_{\gamma_{ac}}$, as shown on Figure 5-1.

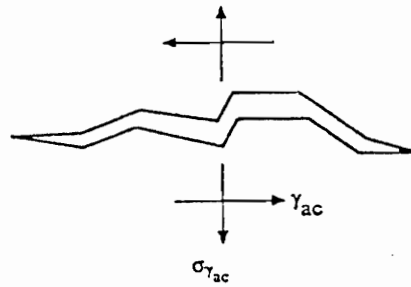


Figure 5-1: Maximum shear stress and associated normal stress around a crack [Socie].

The following relation is given in Bannantine and Socie¹⁶:

$$\gamma_{ac} \left(1 + \frac{\alpha \sigma_{\gamma_{ac}}}{\sigma'_0} \right) = \frac{\tau'_f}{G} (2N_f)^b + \gamma'_f (2N_f)^c \quad (5.7)$$

$$\text{where } \tau'_f = \frac{\sigma'_f}{\sqrt{3}} \quad (5.8)$$

$$\gamma'_f = \sqrt{3} \varepsilon'_f \quad (5.9)$$

$$G = \frac{E}{2(1+\nu)} \text{ is the shear modulus,} \quad (5.10)$$

α is an empirical constant which fulfilled the condition $0.6 < \alpha < 1$ and is used as a factor to represent the importance of the normal stress,

σ'_0 is the cyclic yielding limit, and

b and c are the same fatigue properties as the ones described in the preceding models.

The second term of the right hand side of Equation (5.7) represents the plastic part of the deformation and can be neglected here. The shear strain amplitude, γ_{ac} , can be replaced by the shear stress, τ_{ac} , using:

$$\tau_{ac} = G \gamma_{ac} \quad (5.11)$$

Then the following equation is derived from Equation (5.7):

$$\tau_{ac} \left(1 + \frac{\alpha \sigma_{\gamma ac}}{\sigma'_0} \right) = \tau'_f (2N_f)^b \quad (5.12)$$

Finally, the service life can be expressed by:

$$N_f = \frac{1}{2} \left[\frac{\tau_{ac}}{\tau'_f} \left(1 + \frac{\alpha \sigma_{\gamma ac}}{\sigma'_0} \right) \right]^{\frac{1}{b}} \quad (5.13)$$

From this analysis of the most common fatigue models, three expressions are found for the service life, namely, those given in Equation (5.3), (5.6) and (5.13).

5.2 Selection of the most damaged plane

Of the three fatigue models presented, the first two are used with the effective stress which represents the multiaxial state of stress at a point, and the last one is based on the shear stress. All these stresses are known at several depths for the three different locations around the cam lobe. A procedure is needed to determine the critical plane, i.e. where failure is the most likely to occur, in each location around the lobe. The determination of this peculiar plane or depth is based on a different method for each fatigue model.

For the Morrow model, at each location the stress amplitude, σ_a , and the mean stress, σ_m , are calculated for different depths from the effective stress cycle. The depth where the stress amplitude is the largest is considered as the critical plane, since the amount of change in the stress over one cycle is most important in determining fatigue damage. The value of this stress amplitude, as well as the mean stress at this same depth are used in Equation (5.3) to find the service life following Morrow parameter.

For Smith Watson Topper, a similar routine is used. In each location the maximum stress, σ_{max} , and the stress amplitude, σ_a , are computed for different depths from the effective stress cycle. As before, the depth chosen is the one with the largest stress amplitude. Then this stress amplitude and the corresponding maximum stress are used in Equation (5.6) to predict the service life according to Smith Watson Topper.

Finally, for the Socie model, a comparable procedure is used, only the parameters are changed. At each location, the shear stress, τ_{ac} and the normal stress acting on the plane of this shear are evaluated for several depths. Then, the depth where the magnitude of the shear stress is the highest is chosen as the critical one. This shear stress and the normal stress related to it are used in Equation (5.13) to predict the service life from Socie model.

5.3 Results of the life prediction

By incorporating the calculated lobe stress states into the selected fatigue models, fatigue life predictions are obtained using the procedures described. But, not only a life prediction is desired. It is also essential to determine the failure location, and for that a procedure based on the maximum stress range was developed, as explained in the last section. Then a correlation between the evaluated service life, the failure location and the grinding conditions should be found. These fatigue results also serve as a validation test for the different models, concerning their ability to handle the unusual compressive stress fields characteristic of contact problems.

Life predictions are obtained over a range of maximum Hertzian pressure, p_0 , between 200 and 300 ksi. This range is based on Ford design experience where a typical p_0 is around 230 ksi on the cam lobe. In this part of the work, two other cam lobe are introduced, lobe 4 and 6, in order to cover the complete scale of grinding conditions. Following is an explanation of the results obtained with the selected fatigue parameters. First results are given for the two models which experienced difficulties in a compressive stress environment, SWT and Socie. Then Morrow model, which appears to produce reasonable results, is used to assess cam fatigue performance.

5.3.1 Smith Watson Topper

For this model, the effective stress is used. As noted, the contact involves only compressive stresses. So, the effective stress is also assumed to be a compressive stress. From Equation (5.6), $\sqrt{\sigma_{\max} \sigma_a}$ is a term in the definition of the service life, N_f . σ_a is the stress amplitude, and its value is positive. On the other hand, σ_{\max} , the maximum stress has a negative value. Thus, this product $\sigma_{\max} \sigma_a$ is negative and, because of the square root, gives invalid results. For this reason, the SWT fatigue parameter can not be used for our compressive problem.

5.3.2 Socie

This model is based on the maximum shear stress, τ_{ac} , and the normal stress associated to it, σ_{yac} . Again, for the contact problem, where all the normal stresses are compressive, $\sigma_{\gamma max}$ is also taken compressive. So, this latter stress would have a tendency to close the crack, preventing it from propagating, thereby increasing the service life of this component. In Equation (5.13) is given the definition of N_f according to this model. A parameter α , defined as an empirical constant, appears in the relation. This α is a scale factor on the normal stress and is known from Socie¹⁶ to range between 0.6 and 1. Lacking experimental results, computations are made using two values of α , 1 and 0.6. The range of Hertzian pressure used varies as before from 200 to 300 ksi. These computations are performed first on the base circle of lobe 2, as shown in Table 5-1.

Table 5-1: Life prediction from Socie's model on the base circle of lobe 2 over a range of Hertzian pressure from 200 ksi to 300 ksi.

Pressure (ksi)	200	220	240	260	280	300
Depth of Failure (microns)	25	25	25	25	25	25
Nf Alpha = 0.6 (cycles)	2.70E+04	6.30E+04	1.60E+05	4.60E+05	1.50E+06	4.20E+06
Nf Alpha = 1 (cycles)	5.10E+05	4.00E+06	5.40E+07	1.90E+09	5.00E+11	3.10E+17

A few remarks can be made from this table. The depth of failure appears to always be the same, because, as explained when the computations of the maximum shear stress was done, this is the depth where this stress is maximum. As can be seen in the table, when p_0 gets larger, the life gets longer, which is completely wrong. This can be explained by the fact that when the pressure increases, the normal stress, σ_{yac} , increases at the same time, thus compressing more the cracks and preventing them from propagating, by this way a longer life is obtained. Moreover, in this model, α is a parameter to give more or less importance to the normal stress, σ_{yac} . From the table, it is shown that if α gets larger, the service life increases at the same time. This last point corroborates the preceding remark. It is concluded from these results that the Socie parameter is not a valid model when one works with a compressive stress problem.

5.3.3 Morrow

For this model, the cyclic effective Tresca stress was used in the computation. As before, because in the contact problem all stresses are compressive, the effective stress is assumed to have a negative value. Following are three tables of life predictions for the base circle of lobe 2, lobe 8 and when no residual stresses are considered.

Table 5-2: Life predictions from Morrow parameter at the base circle for (a) lobe 2, (b) lobe 8 and (c) no residual stresses over a range of maximum Hertzian pressure from 200 ksi to 300 ksi.

(a)

Pressure (ksi)	200	220	240	260	280	300
Depth of Failure (microns)	75	100	100	100	100	100
Nf Lobe 2 BC (cycles)	5.30E+08	1.70E+08	8.40E+07	4.60E+07	2.80E+07	1.80E+07

(b)

Pressure (ksi)	200	220	240	260	280	300
Depth of Failure (microns)	100	100	100	125	125	125
Nf Lobe 8 BC (cycles)	1.60E+09	6.50E+08	3.10E+08	1.60E+08	8.20E+07	4.70E+07

(c)

Pressure (ksi)	200	220	240	260	280	300
Depth of Failure (microns)	100	100	100	125	125	125
Nf No RS BC (cycles)	1.60E+09	6.50E+08	3.10E+08	1.60E+08	8.20E+07	4.70E+07

Analyzing these first results, the grinding condition effect can be seen. The burned lobe, lobe 2, results in the shortest lives. The unburned lobe, lobe 8, and the case without residual stress have similar predicted lives. The residual stresses which are weak on the base circle of lobe 8, explain this similarity. Moreover, the tests on the Specialized Vehicles Inc. camshaft test fixture by Ford, are typically run to 1.4×10^8 cycles. After such a test, improperly processed cams will generally fail, which seems in agreement with these first predictions.

Based on these promising results, lobes 4 and 6 are also analyzed. The same computations are done on these lobes (See tables in Appendix C), and a final graph is plotted summarizing these data for the base circle.

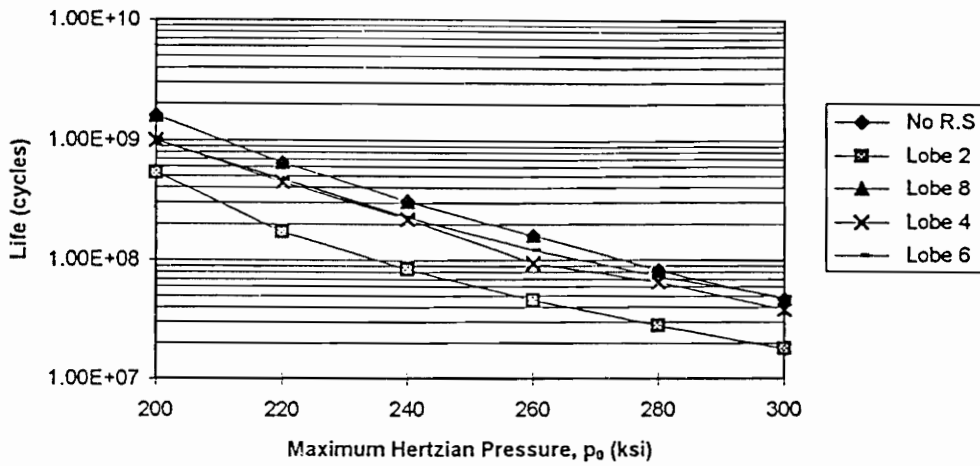
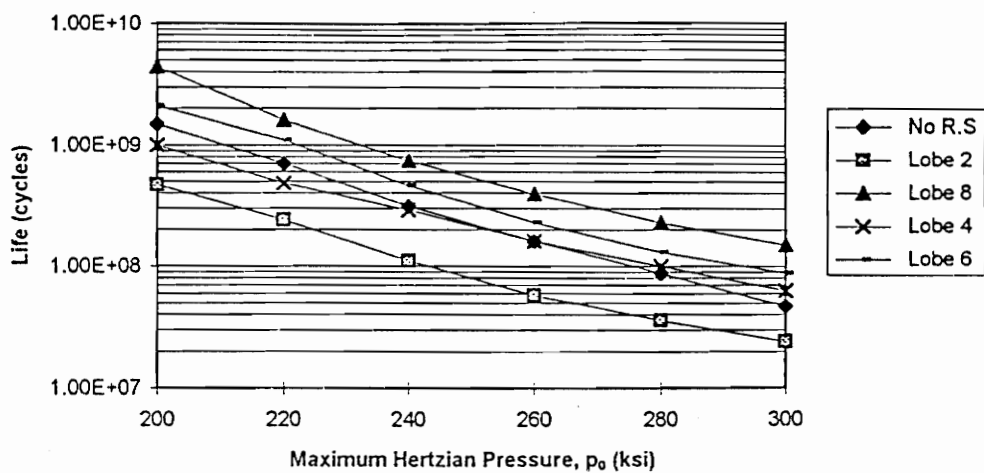
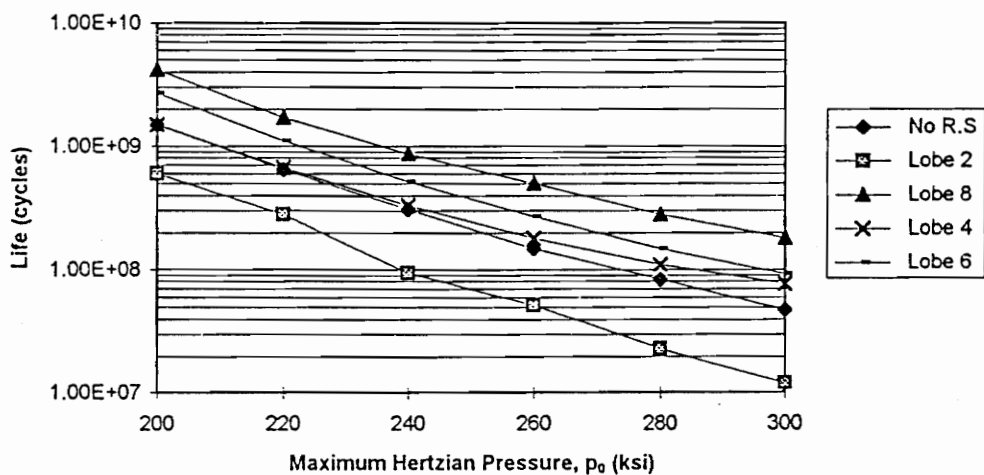


Figure 5-2: Morrow's model predictions on the base circle vs. the maximum Hertzian pressure for several cases.

From Figure 5-2, the lives of the burned lobe (lobe 2) and the unburned one (lobe 8) are seen to differ by a factor of 2 to 3. Thus, the more abusive the grinding, the shorter the life. Lobe 4 and 6, representing intermediate grinding conditions, display intermediate lives. Using the same routine, analyses are performed at the two others locations : the nose and the ramp. These results are presented in the tables in Appendix C and illustrated in the two following graphs, Figure 5-3.



(a)



(b)

Figure 5-3: Morrow's predictions (a) on the nose (b) on the ramp vs. the Hertzian pressure for several cases.

These two graphs are consistent with the earlier trends relating to the grinding conditions. It can be seen that for these two last cases, lobe 6 and 8 (unburned lobes) yield lives even longer

than the case without residual stress. The mild grinding of a cam tends to create subsurface compressive residual stress fields which extend the lifetime presumably by closing the cracks that try to open and propagate. Therefore the compressive subsurface residual stresses are a positive factor on service life.

Concerning the depth of failure predicted, the abusively ground cams tend to fail closer to the surface, due to tensile subsurface residual stresses; this is particularly true for smaller pressures when the residual stress fields play an increasingly important role. For the location of failure, the predicted lives on the base are always similar or shorter than the lives on the ramp and the nose. For these two last locations, the results found are always quite close.

5.3.4 Von Mises effective stress

For all the preceding computations, Tresca effective stress was used. The case of the nose of lobe 2 is reanalyzed but considering the von Mises effective stress, so that a comparison between both criteria can be made. The procedure used is exactly the same, the effective stress is computed over one entire cycle, σ_m and σ_a are calculated and introduced in Morrow model. The results of this calculation appear in Appendix C.

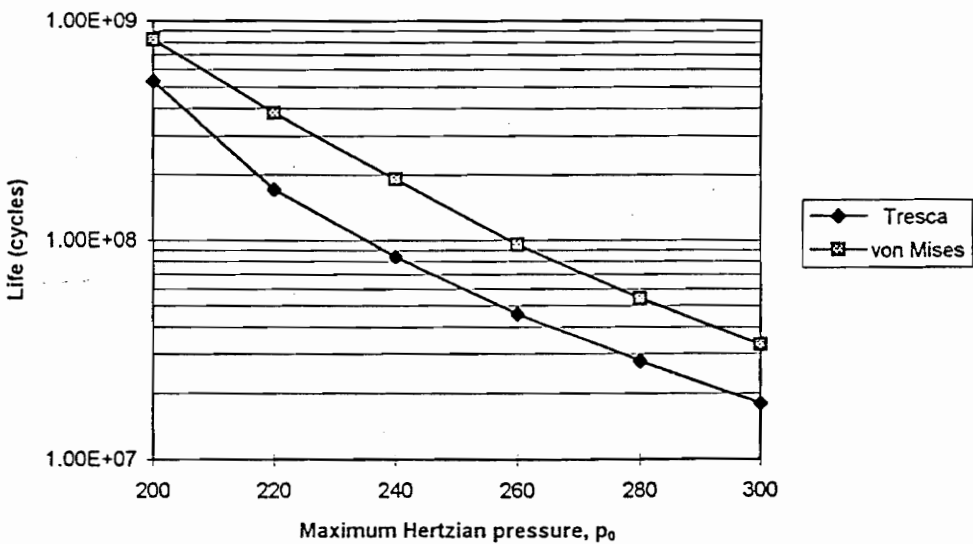


Figure 5-4: Morrow life predictions on the base circle of lobe 2 vs. the maximum Hertzian pressure, using Tresca and von Mises effective stress.

Figure 5-4 shows a comparison between the two effective stresses. For each pressure, the life predicted by von Mises is longer than the life predicted by Tresca, there is always a ratio of at least 1.5 between these two lives. Thus, this graph corroborates what was said earlier about von Mises being more conservative than Tresca. In conclusion, Tresca gives the worse case, so it is safer to consider this criteria.

5.3.5 Assembly residual stress field

During the course of this study, additional x-ray residual stress measurements were received from Ford that included residual stress fields due to assembly. During manufacturing the lobes are pressed on the shafts, thereby creating a residual hoop stress in the cam lobes.

So far, only the residual stress fields due to grinding were considered. Additional computations are done using these new x-ray residual stress measurements to determine their effect on service life. Measurements were made in the circumferential direction on production camshafts that had been ground in usual conditions. These new measurements are compared with the corresponding residual stresses from lobe 4 and 6, which were ground at intermediate conditions. From Figure 5-5, a clear difference is visible between the circumferential residual stress fields, depending if the effect of manufacturing is included or not, especially at depths greater than 75 microns. On the two lobes where only residual stresses from grinding are considered, the value of these stresses decreases significantly, to reach zero when the depth is 125 microns. In comparison, if the residual stresses due to assembly are also considered, these stresses keep a value of 30 ksi until at least a depth of 200 microns.

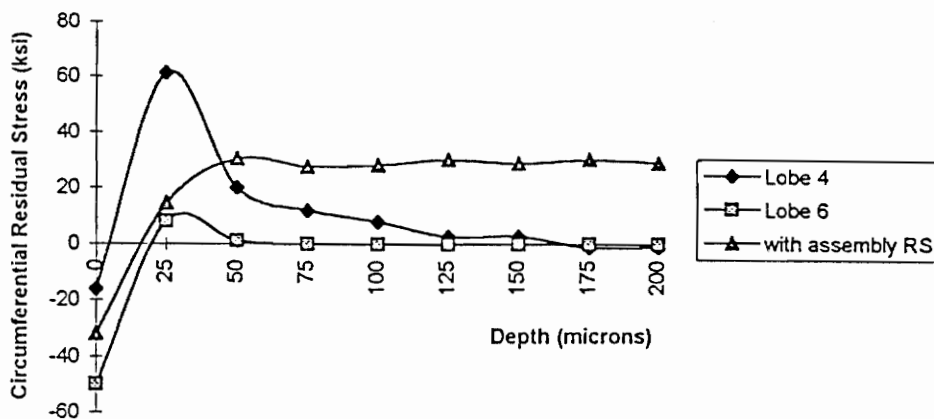


Figure 5-5: Residual stresses in the circumferential direction for lobe 4 and 6 and for Ford data which consider the assembly residual stresses.

These data are then used in conjunction with the axial residual stresses from lobe 4 and 6, to obtain life predictions. In Figure 5-6 the service lives predicted for lobe 4 and 6, with or without the residual stress field due to assembly, are shown.

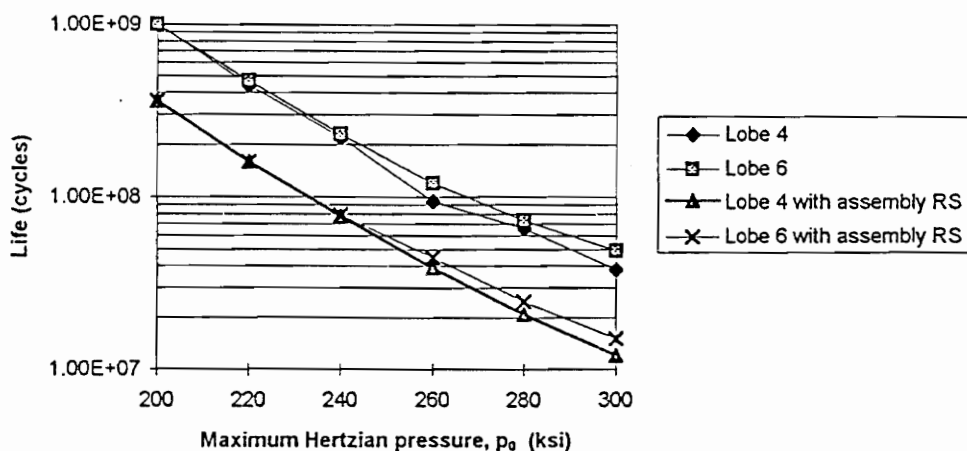


Figure 5-6: Morrow's model predictions on the base circle of lobe 4 and 6 with or without the assembly residual stresses, for a range of maximum Hertzian pressure between 200 ksi and 300 ksi.

As can be seen from this figure, the assembly residual stresses have a significant effect on the fatigue performance, shortening lifetimes by a factor of 4. Thus, these residual stresses should also be considered in the computation of the service life, when they are measurable or calculable, because their effect is not negligible. This also serves to emphasize the value of a reliable predictive model for quickly estimating the effects, on fatigue life, of a range of processing and performance parameters.

6. DISCUSSION

The preceding sections illustrate the characterization of the contact stress state by using an extended Hertzian method which, when combined with the residual stresses, provides the operative stress field. Effective stresses are computed to evaluate possible yielding and find the maximum cyclic component; thus, lifetimes are predicted for differently ground cam lobes. In this section, implications and future applications of the different elements of the analysis are discussed.

From the stress analysis, the Hertzian method extended by Smith and Liu² is demonstrated to be a reliable tool to characterize the contact stress state. This permits the determination of the failure location, generally subsurface, and provides the necessary stress information for life estimation. 3-D mappings of these different contact stresses allow a better presentation and understanding of the stress variations. For example, using this kind of mapping, it is clearly seen that the maximum shear stress value is subsurface.

In addition, by considering residual stresses due to manufacturing and assembly, the problem is brought closer to reality. Often these stresses are neglected, but they are present in numerous components and their effect may be quite significant. Elastic superposition of the contact stress field with the residual stress field gives the actual multiaxial stress field in the cam required for accurate lifetime predictions. When performing this multiaxial superposition, the directionality both stress fields must be maintained.

In this first part, only elastic behavior was assumed. A plasticity analysis using conventional multiaxial yield criteria (Tresca and von Mises) indicates that yielding might be anticipated in abusively ground lobes. It is expected that this could result in an initial redistribution of the residual stresses, but that the cyclic stresses would remain elastic. Camshafts have a very long life, therefore cyclic yielding should be negligible for this component. The initial redistribution of the residual stress fields occurs through cyclic relaxation and can be characterized by a simple

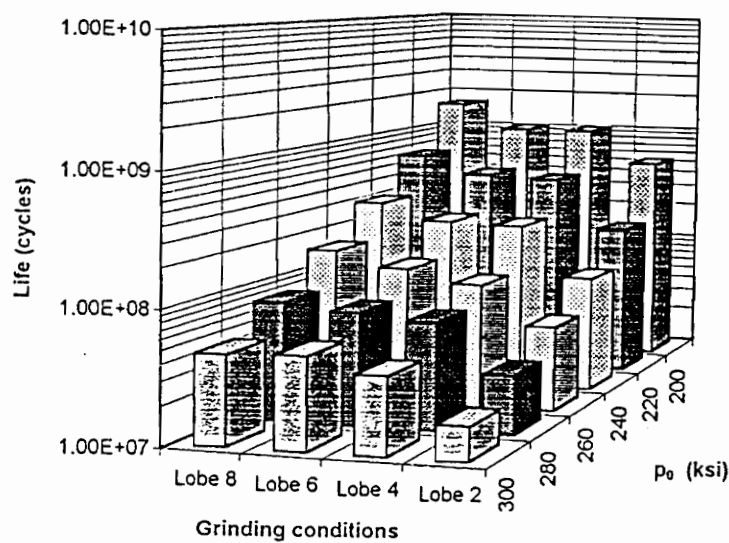
model. However, this model represents the worse case of relaxation, the actual relaxation would likely be less than predicted.

A unique characteristic of contact problem is a complete compressive stress field. Compression is an uncommon situation and accounts for the failure of SWT and Socie models to predict valid lifetimes. On the other hand, Morrow model gives satisfactory service lives in this environment. To find the failure location, an observation of the effective stress amplitude at each depth is performed thus, leading to a predicted location function for the combined stress fields.

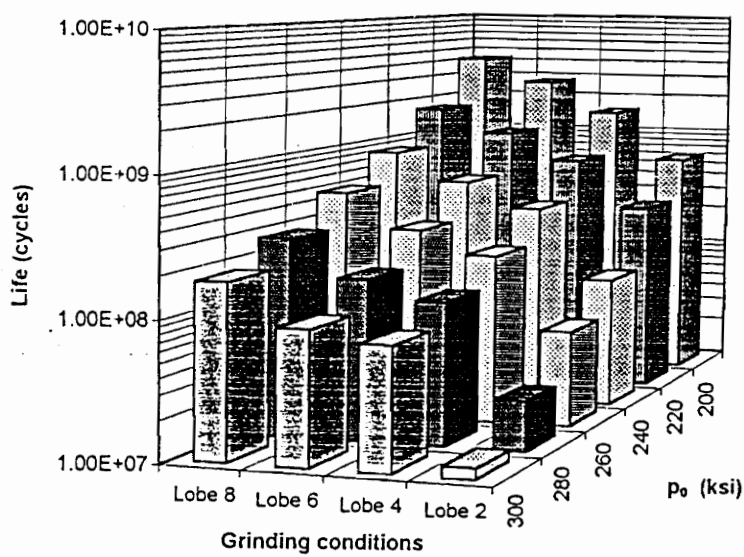
Fatigue tests are planned using the Specialized Vehicles Inc. camshaft test fixture. Lifetimes and failure locations will be determined and x-ray measurements of the residual stresses after testing will be executed to check the relaxation assumption. Unfortunately, no tests have been run yet, due to numerous delays.

Using the Morrow model for lobes ground under various conditions, fatigue lives can be determined, thus correlation between grinding and service life can be found. In the 3-D graphs seen in Figure 6-1, these life predictions are shown as a function of the maximum Hertzian pressure, p_0 , and the grinding conditions. Recall that lobe 2 received the most abusive grinding. Such 3-D graphs could serve as a link between the requirements of the design (through p_0) and those of the manufacturing operations (through the grinding conditions). Knowing the characteristics desired from the camshaft, its expected service life, decisions can be made concerning allowable grinding protocols and service stress levels necessary to achieve desired performances.

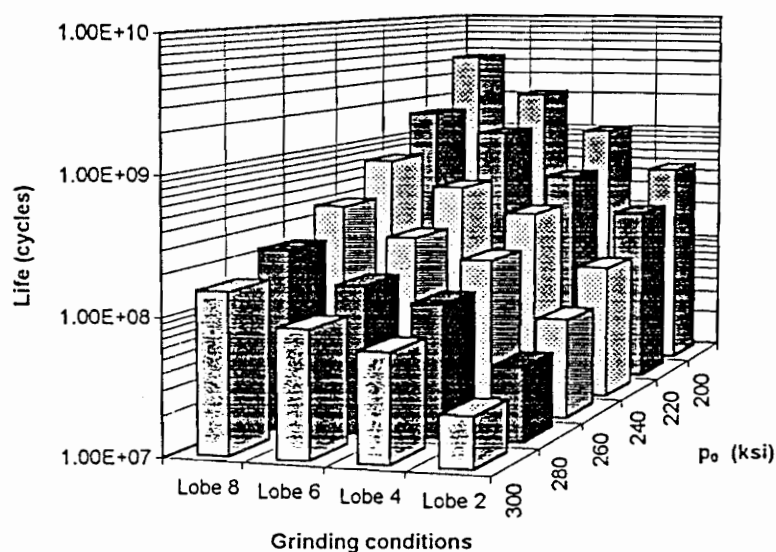
The following trends are apparent from these graphs. If the Hertzian pressure is increased by 100 ksi, the life is reduced by a factor of twenty. The life also follows this tendency when the grinding is rougher. Thus, the more abusive the grinding, the shorter the life. For example, there is a factor of 15 on the life between the ramp of lobe 2 and lobe 8 when a Hertzian pressure of 300 ksi is considered. For gently ground lobes, the life is increased through creation of a compressive subsurface residual stress field which prevents crack growth. Therefore, gentle grinding could be a positive factor to obtain longer life, but it necessitates more grinding passes and so diminishes the production rates.



(a)



(b)



(c)

Figure 6-1: Life predictions according to Morrow model as a function of the grinding conditions and the maximum Hertzian pressure (a) on the base circle, (b) on the ramp and (c) on the nose.

The location of failure is subsurface, as predicted by the Hertzian analysis, but this location is closer to the surface for more abusive grinding due to the high tensile stress field present just below the surface, as demonstrated in Table 6-1.

Table 6-1: Failure locations below the surface on the base circle over a range of pressure between 200 ksi and 300 ksi for the different lobes.

Pressure (ksi)	200	220	240	260	280	300
Lobe 2 (microns)	75	100	100	100	100	100
Lobe 4 (microns)	100	100	100	100	150	150
Lobe 6 (microns)	100	100	125	125	125	150
Lobe 8 (microns)	100	100	100	125	125	125

Then, a comparison between the three locations (nose, ramp and base circle) leads to the conclusion that the shortest lives are found on the base circle and the ramp, especially for the burned lobe (lobe 2). Here it must be noted that the predictions are done for the same pressure range for the three locations, because the dynamic loads are unknown. A rapid dynamic analysis had been done by Moeller, according to the method demonstrated by Norton²¹. From this, dynamic

loads were obtained around the cam lobe for several speeds of rotation of the camshaft, as illustrated in Figure 6-2.

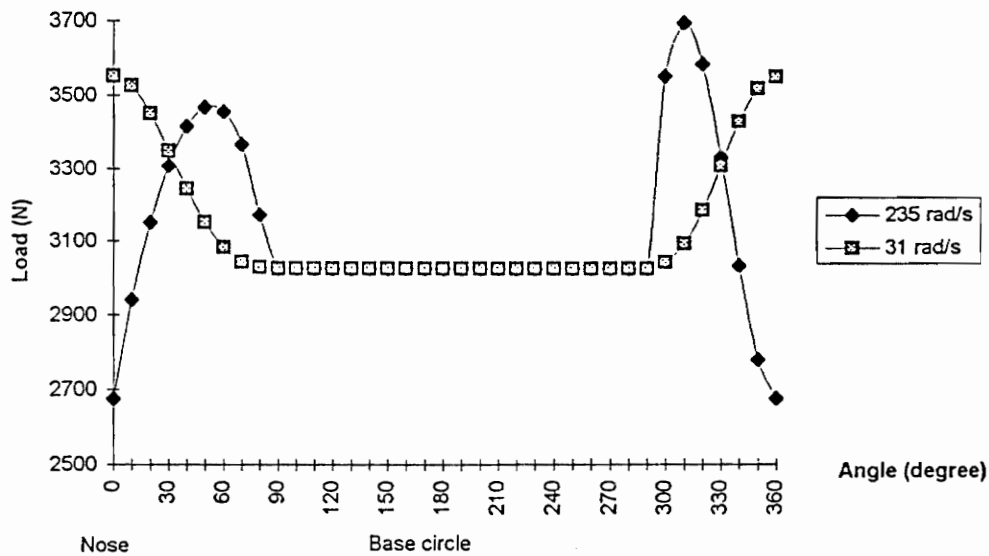


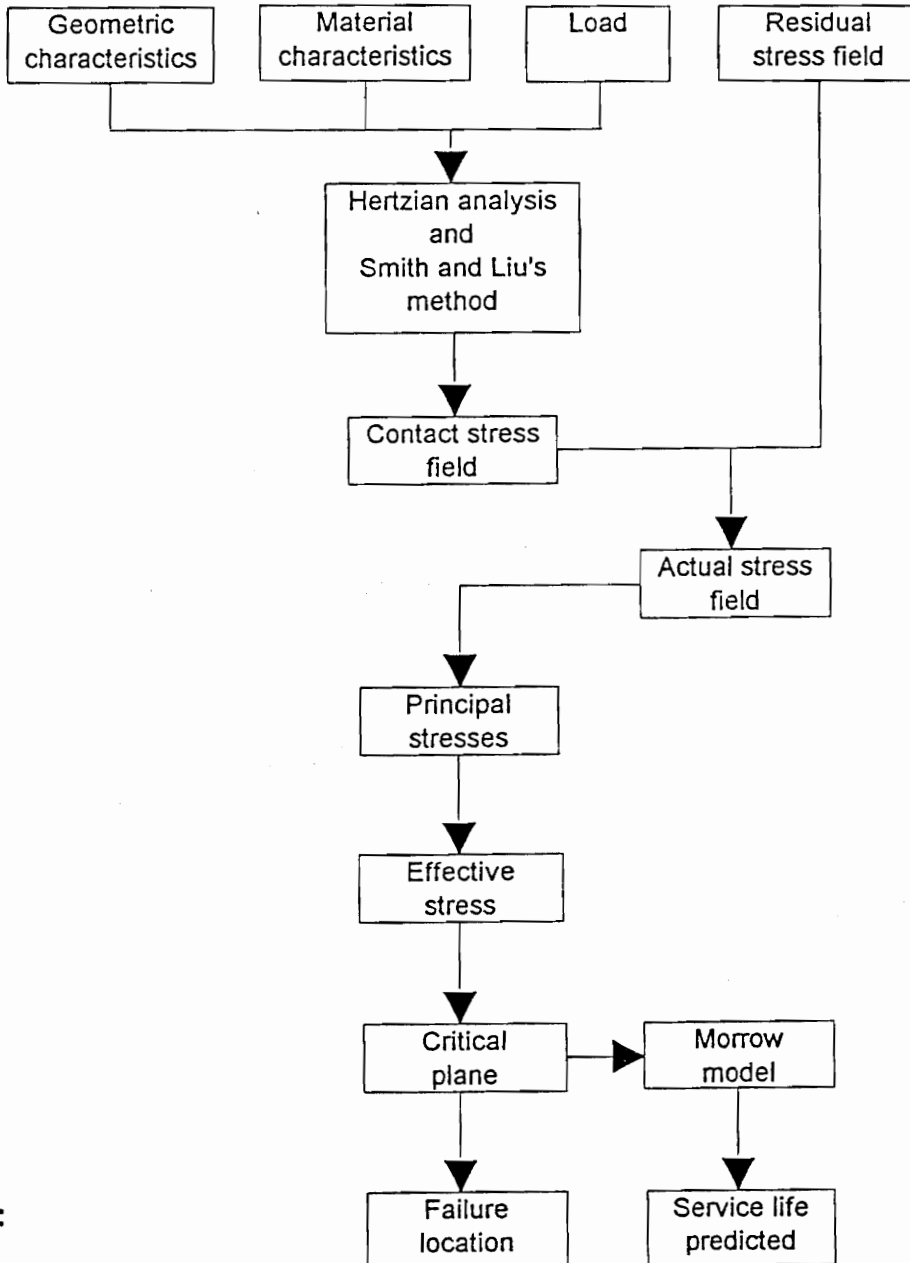
Figure 6-2: Loads around the cam lobe caused by the valve train for two camshaft rotation speeds.

Dynamic loads are obviously varying around the cam lobe depending of the rotation speed of the camshaft, so that the Hertzian pressure applied on the cam is different in each location. Thus, using the exact dynamic loads linked to the valve train considered in this work, quite different service lives will be found for the nose, the ramp and the base circle. When available, such information can be easily accommodated in the life prediction routine.

Finally, a tool has been developed to help understanding the effect of each parameter on the final fatigue life. This is a routine, written in Mathcad, summarizing all the procedures used in this work, whose structure is outlined in Table 6-2. To use this routine, a few inputs have to be specified, then the precedent scheme is followed, and the outputs are the predicted life and failure location. If the dynamic analysis of the valve train is done, it can simply be added to this routine, replacing the load input. The advantage of this tool is its adaptability and speed. Thus, if new information is given about one of the inputs, updated results can be obtained rapidly. This was the case for the new x-ray measurements given by Ford about the assembly residual stresses; a few adaptations were made and new life predictions were obtained in a short time. Therefore, this tool could of considerable use to designers in understanding the effects of various manufacturing and design parameters on cam performance. Such tools are consistent with industrial trends placing greater reliance on analytical design aids.

Table 6-2 : Structure of the routine developed.

Inputs :



Outputs :

7. CONCLUSIONS

7.1 Conclusions

Based on the results of this study of a cam-roller follower system, the following conclusions can be drawn:

- A Hertzian type analysis, as extended by Smith and Liu, provides a complete 3-D documentation of the stress state in the contact zone and allows identification for the fatigue calculations, of the maximum cyclic stress component which generally occurs subsurface.
- Preexisting stress fields due to manufacturing and assembly can be combined through superposition with the contact stresses to obtain the operative stress field. In performing this superposition, it is important to maintain the directionality of the individual stress components.
- Plasticity, as determined by conventional yield criteria, is found on the most abusively ground lobes but only during the initial loading cycle. Cyclic relaxation of the residual stresses according to analysis, could be a possibility and needs to be corroborated by experimental results.
- Two of the fatigue models, SWT and Socie are found to be inappropriate for the completely compressive contact stress fields. The Morrow model demonstrates its capacity to work in such a compressive environment, by giving reasonable life estimates. The availability of a reliable life prediction model allows sensitivity analyses to be performed to account for the effects of the variations of grinding protocol, dynamic loading or material properties on the fatigue life. In this way, a basis for optimizing cam performance is accessible to engine designers.

- The apparent success of this predictive model provides a basis for extending the analysis to other contact problems, e.g. gears and bearings, and is consistent with industrial trends towards greater reliance on analytical design and evaluation tools.

7.2 Recommendations

Recommendations for future work are as follow:

- Fatigue tests of assembled camshafts prepared under varying grinding protocols, should be performed in order to corroborate the estimated lifetimes and failure locations, as well as to check the occurrence of residual stress relaxation.
- Finite element model could provide useful information concerning the “edge effect”, i.e. the transition from plane stress to plane strain conditions, and the onset of plastic deformation. Frictional effects could also be included in such model.
- Dynamic modeling of the valve train would provide analytical estimates of the loads on the cam as a function of the speed of rotation and the valve spring stiffness and enable more precise life predictions for each location on the cam (e.g. nose, ramp, base circle).
- A more complete material property characterization of the AISI 52100 steel, in order to assess possible variations due to heat treatment and the operating temperatures present in actual engines, would provide further analysis refinements.

8. REFERENCES

- ¹ Hertz, H.R., *J. Reine Angew. Math.* (Crelle's J.), vol. 92, pp. 156-171 (1881) or Hertz, H.R., *Miscellaneous Papers*, pp. 146-162, Jones and Schott, London 1896.
- ² Smith, J.O. and Liu, C.K., "Stresses due to Tangential and Normal Loads on an Elastic Solid with Application to some Contact Problems," *Journal of Applied Mechanics*, vol. 20, pp.157-166, June 1953.
- ³ Moyer, G.J. and Morrow, J.D., "Surface Fatigue Research of Bearings and Other Rolling Elements," *Engineering Experiment Station Bulletin*, No. 468, University of Illinois, 1964.
- ⁴ Littman, W.E. and Widner, R.L., "Propagation of Contact Fatigue From Surface and Subsurface Origins," *ASME Transactions Series*, vol. 88, pp. 624-636, 1966.
- ⁵ Keer, L.M. and Mura, T., "A Contact Problem for the Elastic Quarter Space," *International Journal of Solids Structure*, vol. 20, No. 5, pp. 513-524, 1984.
- ⁶ de Mul, J.M. and Kalker, J.J., "The Contact Between Arbitrarily Curved Bodies of Finite Dimensions," *Transactions of the ASME*, vol. 108, pp. 140-148, 1986.
- ⁷ Shukla, A. and Nigam, H., "A Numerical-Experimental Analysis of the Contact Stress Problem," *Journal of Strain Analysis*, vol. 20, No. 4, pp. 241-245, 1985.
- ⁸ Hahn, G.T. and Bhargava, V., "Analysis of the Rolling Contact Residual Stresses and Cyclic Plastic Deformation of SAE 52100 Steel Ball Bearings," *Transactions of the ASME*, vol. 109, pp. 618-626, 1987.
- ⁹ Hearn, E.J., *Mechanics of Materials*, pp. 777-831, Pergamon Press 1985.
- ¹⁰ Juvinall, R.C., *Stress, Strain and Strength*, pp. 370-397, McGraw-Hill 1967.
- ¹¹ Liebowitz, H., *Fracture, an Advanced Treatise*, vol. 2, pp. 316-348, New York, Academic Press 1968.
- ¹² Johnson, W. and Mellor, P.B., *Engineering Plasticity*, pp. 63-99, Ellis Horwood Limited 1983.
- ¹³ Dowling, N.E., *Mechanical Behavior of Materials*, pp. 233-275, Prentice Hall 1993.
- ¹⁴ Baeunel, A. and Seeger, T., *Materials Data for Cyclic Loading*, Fachgebiet Werkstoff Mechanik Technische Hochschule, Darmstad 1988.
- ¹⁵ Leese, G.E. and Socie, D., *Multiaxial Fatigue : Analysis and Experiments*, pp. 67-80, Society of Automotive Engineers 1989.
- ¹⁶ Bannantine, J.A. and Socie, D.F., "A Variable Amplitude Multiaxial Fatigue Life Prediction Method," *Fatigue under Biaxial and Multiaxial Loading*, ESIS10, 1991, Mechanical Engineering Publications, London, pp. 35-51.
- ¹⁷ Socie, D. "Multiaxial Fatigue Damage Models," *Journal of Engineering Materials and Technology*, ASME, vol. 109, October 1987, pp. 293-298.

-
- ¹⁸ Fatemi, A. and Socie, D.F., "A Critical Plane Approach to Multiaxial Fatigue Damage Including Out-of-Phase Loading," *Journal of Engineering Material Structures*, vol. 11, No. 3, pp. 149-165, 1988.
- ¹⁹ Courtney, S.B., *A Rapid Non-Destructive Test to Detect Camshaft Lobe Grinding Burn*, Master of Science Thesis, Virginia Polytechnic Institute, December 1993.
- ²⁰ Landgraf, R.W. and Chernenkoff, R.A., "Residual Stress Effects on Fatigue of Surface Processed Steels," *Analytical and Experimental Methods for Residual Stress Effects in Fatigue*, ASTM STP 1004, R.L. Champoux, J.H. Underwood and J.A. Kapp Eds., American Society for Testing and Materials, Philadelphia 1988, pp. 1-12.
- ²¹ Norton, R.L., *Design of Machinery*, McGraw Hill Inc., New-York 1992.

9. APPENDIX A : MATERIAL PROPERTIES OF AISI 52100

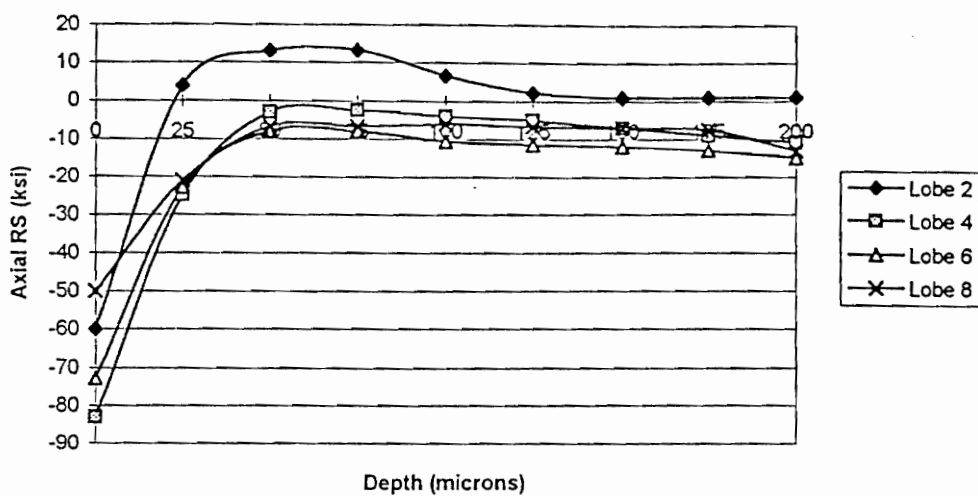
Monotonic properties:

- Young's modulus: $E = 206\,700\text{ N/mm}^2$
- Yield strength (0.2 %): $\sigma_0 = 1922\text{ N/mm}^2$
- Poisson's ratio: $\nu = 0.29$

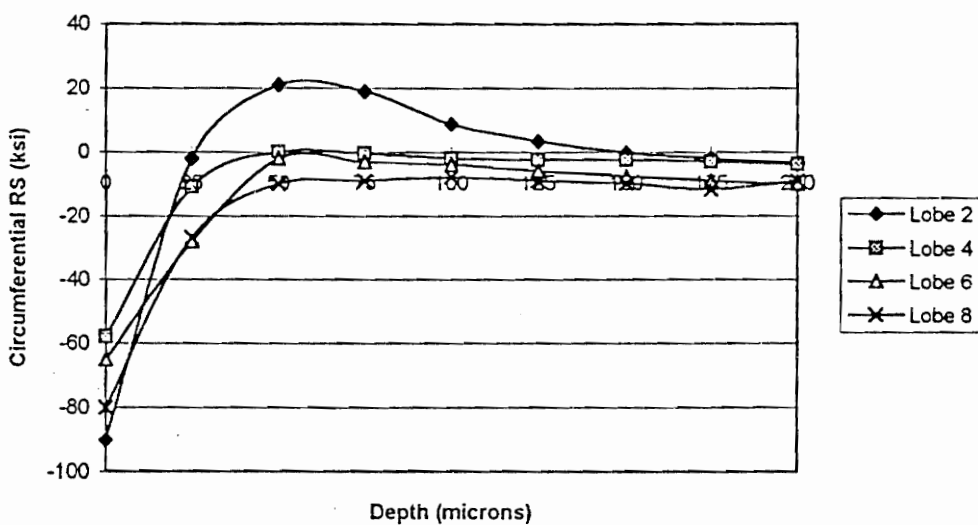
Cyclic properties:

- Yield strength (0.2 %): $\sigma'_0 = 1336\text{ N/mm}^2$
- Fatigue properties: $\sigma'_f = 2725\text{ N/mm}^2$
 $\varepsilon'_f = 0.240$
 $b = -0.097$
 $c = -0.638$

10. APPENDIX B : RESIDUAL STRESS GRAPHS

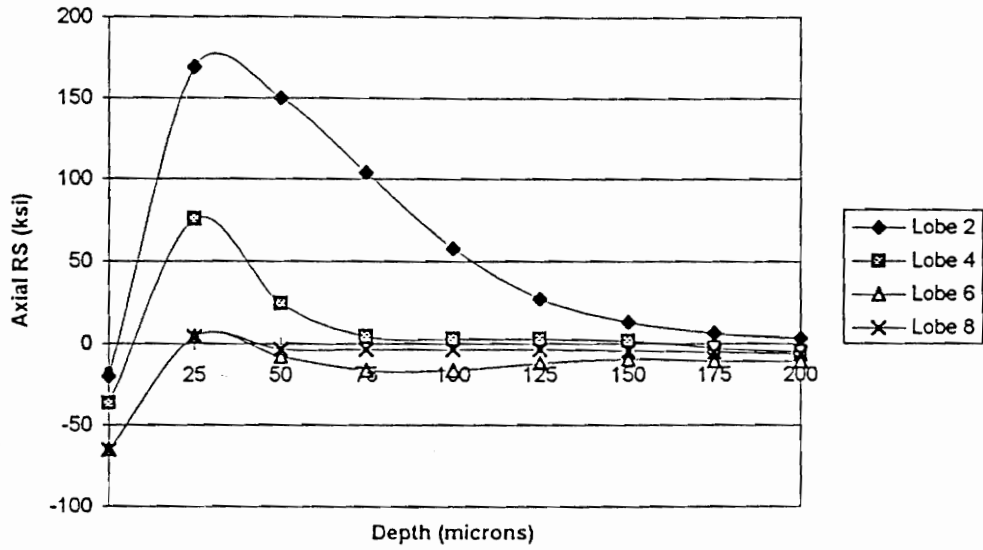


(a)

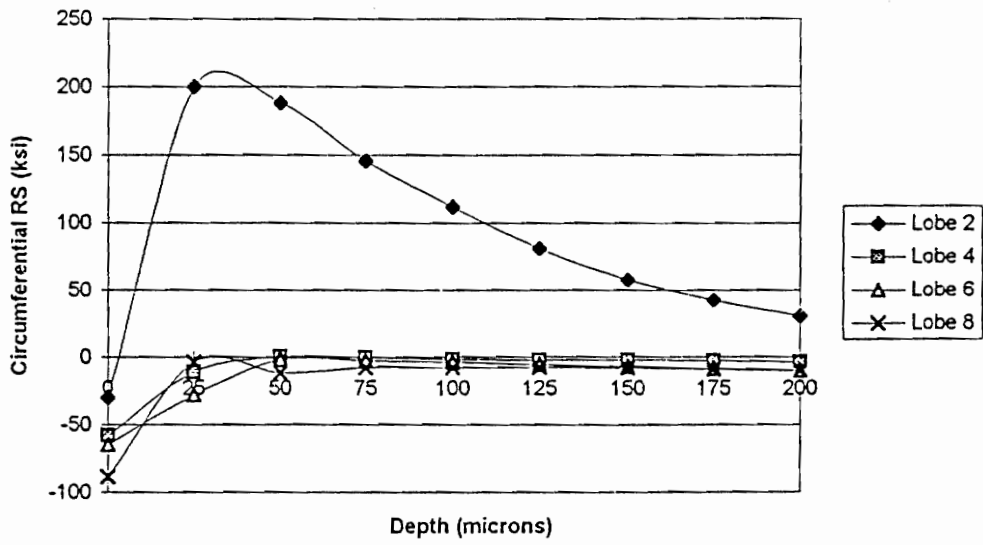


(b)

Figure 10-1: (a) Axial and (b) circumferential residual stresses vs. depth on the nose of the different lobes [Courtney].

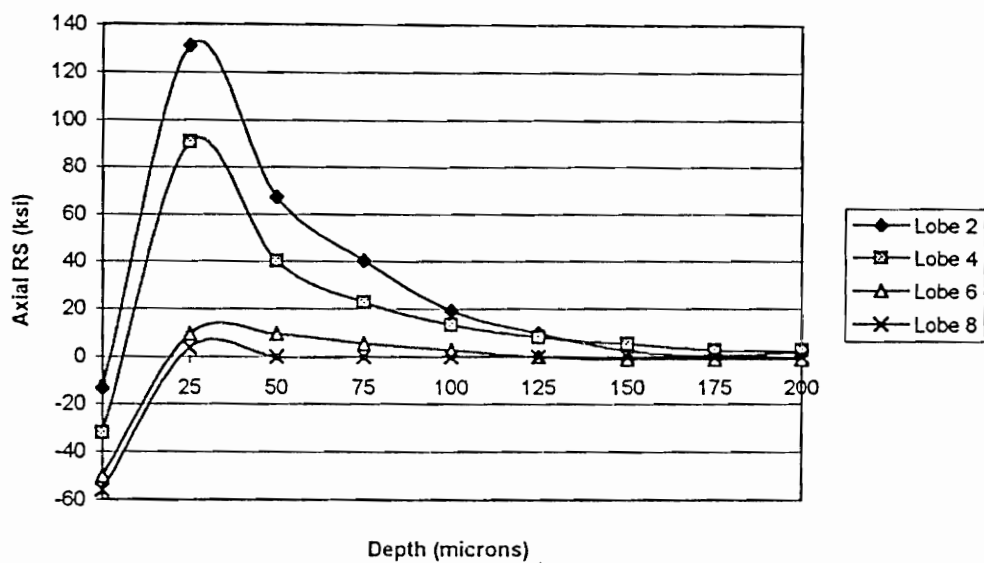


(a)

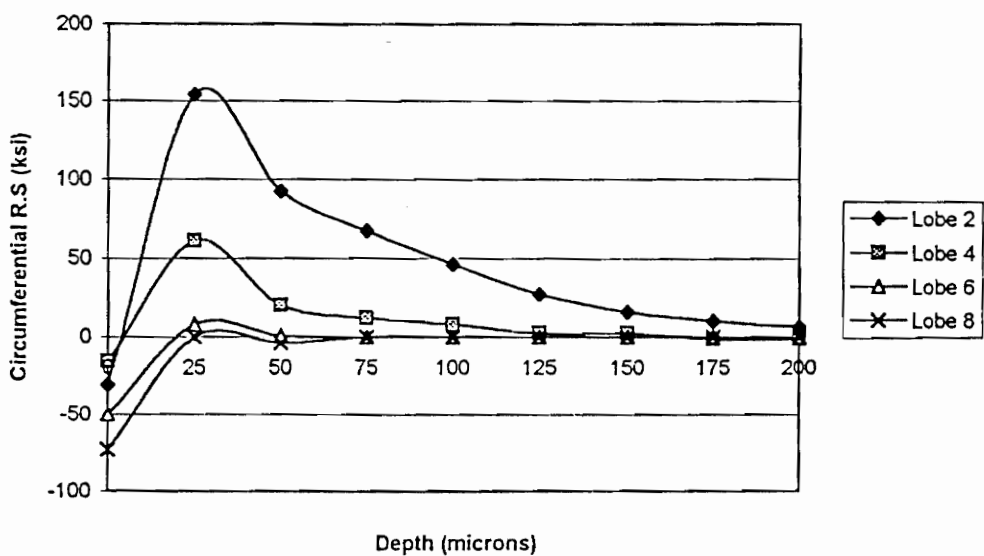


(b)

Figure 10-2: (a) Axial and (b) circumferential residual stresses vs. depth on the ramp of the different lobes [Courtney].



(a)



(b)

Figure 10-3: (a) Axial and (b) circumferential residual stresses vs. depth on the base circle of the different lobes [Courtney].

11. APPENDIX C : TABLES OF PREDICTED SERVICE LIVES

Table 11-1: Service life predictions from Morrow model on the nose.

Lobe 2

Pressure (ksi)	200	220	240	260	280	300
Depth of Failure (microns)	75	75	100	100	100	100
Nf Lobe 2 N (cycles)	4.70E+08	2.40E+08	1.10E+08	5.80E+07	3.60E+07	2.40E+07

Lobe 4

Pressure (ksi)	200	220	240	260	280	300
Depth of Failure (microns)	75	75	100	100	125	125
Nf Lobe 4 N (cycles)	1.00E+09	4.80E+08	2.90E+08	1.60E+08	1.00E+08	6.30E+07

Lobe 6

Pressure (ksi)	200	220	240	260	280	300
Depth of Failure (microns)	75	100	100	100	100	100
Nf Lobe 6 N (cycles)	2.10E+09	1.10E+09	4.60E+08	2.30E+08	1.30E+08	8.70E+07

Lobe 8

Pressure (ksi)	200	220	240	260	280	300
Depth of Failure (microns)	100	100	100	100	100	125
Nf Lobe 8 N (cycles)	4.40E+09	1.60E+09	7.40E+08	3.90E+08	2.30E+08	1.50E+08

No RS

Pressure (ksi)	200	220	240	260	280	300
Depth of Failure (microns)	75	100	100	100	125	125
Nf No RS N (cycles)	1.50E+09	7.00E+08	3.10E+08	1.60E+08	8.70E+07	4.70E+07

Table 11-2: Service life predictions from Morrow model on the ramp.

Lobe 2

Pressure (ksi)	200	220	240	260	280	300
Depth of Failure (microns)	125	125	150	150	175	200
Nf Lobe 2 R (cycles)	6.00E+08	2.80E+08	9.40E+07	5.20E+07	2.30E+07	1.20E+07

Lobe 4

Pressure (ksi)	200	220	240	260	280	300
Depth of Failure (microns)	150	175	175	175	175	200
Nf Lobe 4 R (cycles)	1.50E+09	6.70E+08	3.30E+08	1.80E+08	1.10E+08	7.70E+07

Lobe 6

Pressure (ksi)	200	220	240	260	280	300
Depth of Failure (microns)	150	150	175	200	200	200
Nf Lobe 6 R (cycles)	2.70E+09	1.10E+09	5.20E+08	2.70E+08	1.50E+08	9.20E+07

Lobe 8

Pressure (ksi)	200	220	240	260	280	300
Depth of Failure (microns)	150	150	150	175	175	200
Nf Lobe 8 R (cycles)	4.20E+09	1.70E+09	8.60E+08	5.00E+08	2.80E+08	1.80E+08

No RS

Pressure (ksi)	200	220	240	260	280	300
Depth of Failure (microns)	150	150	175	175	200	225
Nf No RS R (cycles)	1.50E+09	6.50E+08	3.10E+08	1.50E+08	8.30E+07	4.80E+07

Table 11-3: Service life predictions from Morrow model on the base circle.

Lobe 2						
Pressure (ksi)	200	220	240	260	280	300
Depth of Failure (microns)	75	100	100	100	100	100
Nf Lobe 2 BC (cycles)	5.30E+08	1.70E+08	8.40E+07	4.60E+07	2.80E+07	1.80E+07

Lobe 4						
Pressure (ksi)	200	220	240	260	280	300
Depth of Failure (microns)	100	100	100	100	150	150
Nf Lobe 4 BC (cycles)	1.00E+09	4.40E+08	2.20E+08	9.40E+07	6.60E+07	3.80E+07

Lobe 6						
Pressure (ksi)	200	220	240	260	280	300
Depth of Failure (microns)	100	100	125	125	125	150
Nf Lobe 6 BC (cycles)	1.00E+09	4.70E+08	2.30E+08	1.20E+08	7.30E+07	4.90E+07

Lobe 8						
Pressure (ksi)	200	220	240	260	280	300
Depth of Failure (microns)	100	100	100	125	125	125
Nf Lobe 8 BC (cycles)	1.60E+09	6.50E+08	3.10E+08	1.60E+08	8.20E+07	4.70E+07

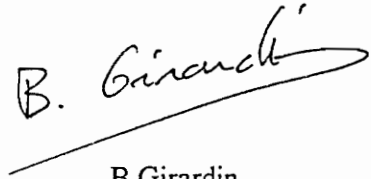
No RS						
Pressure (ksi)	200	220	240	260	280	300
Depth of Failure (microns)	100	100	100	125	125	125
Nf No RS BC (cycles)	1.60E+09	6.50E+08	3.10E+08	1.60E+08	8.20E+07	4.70E+07

Table 11-4: Service life predictions from Morrow model using von Mises effective stress on the nose of lobe 2.

Lobe 2						
Pressure (ksi)	200	220	240	260	280	300
Depth of Failure (microns)	75	75	75	100	100	100
Nf Lobe 2 N (cycles)	8.20E+08	3.80E+08	1.90E+08	9.50E+07	5.40E+07	3.30E+07

VITA

The author was born on August 13, 1970, in Saint Dizier, France. He spent all his childhood in the family farm in a small village of the French countryside, where he had some happy years in the middle of his family. After completing high-school, he pursued his studies at the "Université de Technologie de Compiègne (U.T.C)", France, in the Mechanical Engineering department. During these four years in Compiègne, he met some wonderful friends and took advantage of his student life. An opportunity to go to graduate school in the USA, being offered, the author arrived in Blacksburg in August 1992, to pursue a Master's program in the Engineering Science and Mechanics department of Virginia Tech. After completing the requirements for a Master's Degree, he will receive at the same time his French "Diplôme d'ingénieur". The author will start his military service during the fall 1994 and look for a job one year later.

A handwritten signature in black ink, reading "B. Girardin". The signature is written in a cursive style with a long horizontal line extending from the end of the name.

B.Girardin.